Dopant effects on solid-solid transitions in atomic clusters

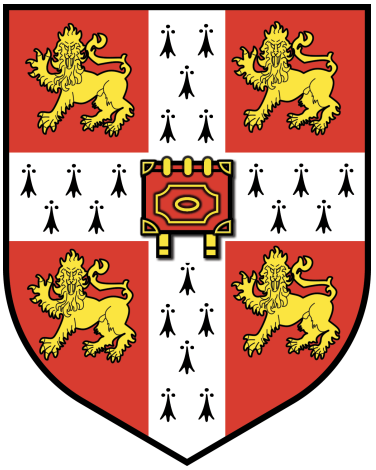

Brooke Elena Husic

Churchill College

August 2015

This dissertation is submitted to the University of Cambridge

for the degree of Master of Philosophy

Abstract

Multicomponent atomic clusters (i.e. nanoalloys) are currently a subject of intense interest because their properties can be tuned by adjusting the cluster size and composition. Previous work has demonstrated the sensitivity of cluster structure and melting temperature to the presence of a single dopant atom. This thesis theoretically examines the effect of a single dopant on the solid-solid transitions of LJ clusters characterised by a double-funnel energy landscape. The incorporation of a dopant atom into LJ_{38} or LJ_{31} offers a tunable change in the transition temperature between two competing solid states by influencing the potential energy and vibrational entropy of low-lying minima. A two-state approximation is utilised to calculate the solid-solid transition temperatures and is shown to agree with trends in heat capacity features even when only one minimum is used to describe each solid state. The observed sensitivity of preferred cluster geometry to a single dopant and resulting trends in solid-solid transition temperature provide a theoretical precursor for the structural control of solid-state nanoalloys.

Declaration

This dissertation is the result of my own work and includes nothing which is the outcome of work done in collaboration except where specifically indicated in the text. This dissertation has not been submitted for any other degree or qualification at this or any other university, and does not exceed 15,000 words in length.

Brooke Elena Husic

August 2015

Acknowledgements

I must first thank my supervisor, David Wales, for his guidance and support from my application to Cambridge through (and beyond) the completion of this dissertation. His encouragement of curiosity-driven research led me down an unplanned path which ultimately resulted in the findings of this thesis. I must also thank Dr. Dmitri Schebarchov, whose insight and mentorship throughout this project have been invaluable to my research and development as a scientist. I am grateful to all the other members of the Wales Group, especially Dr. Cheng Shang, Dr. Chris Forman, Dr. Chris Whittleston, Dr. Jo Carr, James Farrell, Kyle Sutherland-Cash and Sam Niblett for various discussions and suggestions. I also thank Stefano Martiniani for his help with the HSA derivation and throughout the year.

I am inexpressibly grateful for the support of my friends and family. I am especially thankful to Ally Freedy, Jerelle Joseph, László Seress and Reid Lidow for their friendship and guidance. I also thank Brian Feldman and Tianqi Wang, both of whom visited me in Cambridge, for important conversations and friendships that have continued to strengthen since our graduations from Wash. U. Most of all, I am thankful for the constant support and love from my family (Mom, Dad, Will), who support my academic endeavours even when they take me overseas, and from my f.b.m. Derrick, who has always believed in me and continues to inspire me to become the best version of myself.

I am grateful to the Gates Cambridge Trust for the award of a Gates Cambridge Scholarship and the opportunity to study at the University of Cambridge. Finally, I must thank Dr. Howie Breinan and Dr. Jay Ponder, who expected more of me than I knew to expect of myself, and whose encouragement in the early stages of my career have provided the foundation for present and future academic success.

This thesis is dedicated to my mom and role model,

Donna-Lee Husic.

Table of abbreviations

Abbreviation	Definition
fcc	face-centred cubic
HSA	harmonic superposition approximation
icos	icosahedral
Ino-dodec	Ino-dodecahedral
LJ	Lennard-Jones
LJ_N	the Lennard-Jones cluster containing N atoms
$\mathrm{LJ}_N^{(i)}$	the ith lowest minimum of homogeneous LJ_N
MD	molecular dynamics
PES	potential energy surface

Glossary of selected[†] symbols

Symbol	Definition
A, B	binary LJ atom type
a	local minimum
α, β	set of minima associated with a state
ε	LJ 'stickiness' parameter
F	free energy
i, j	minimum index
N	number of atoms
N_{nn}	number of nearest neighbours
σ	LJ size parameter
T_{ss}	solid-solid transition temperature
V	potential energy
V_{strain}	strain energy
Z	partition function
Ω	classical density of states

[†]The symbols enumerated in the glossary are limited to those used in the text without restatement of context or meaning.

Contents

1 Introduction

1.1 Nanoalloys

Bimetallic nanoparticles, or nanoalloys, have been the subject of recent research in materials science, chemistry, biology, and medicine due to their structural and catalytic properties.[1–9] Nanoalloy catalysts, for example, have been shown to resist deactivation, which is observed in the pure alloy constituents.[3,4] The properties of nanoalloys can be programmed not only by adjusting their size, as with homogeneous metallic clusters, but also by modifying their composition. The past decade has seen many theoretical investigations of nanoalloys and their properties, which can inform the understanding of more complex physical systems.[8,10–26] The nature of phase transitions in nanoalloys has been one such property of interest, and several studies have demonstrated the effects of nanoalloy composition on the melting temperature of a nanocluster. Homogeneous nanocluster melting temperatures have been shown to both decrease[16,20,22,27] and increase[13,21,22,24] due to changes in the amount or type of dopant atoms. Both Lyalin et al.[27] and Mottet et al.[13] have demonstrated that exchange of a single atom in a homogeneous cluster for a dopant atom of different identity is sufficient to lower or raise the melting temperature of the cluster, respectively. The incorporation of a single dopant atom into a nanocluster has also been shown to change its solid-state structure.[11,18]

In order to understand and predict the phase transition behaviour and other thermodynamic properties of nanoalloys, the minimum energy structure must be identified. Locating low-lying minima is more difficult for binary systems than for their homogeneous counterparts due in part to the complication of compositional ordering, i.e. the existence of multiple structures with nearly identical geometric motifs

but different arrangements of component atoms, which are called homotops[10] or permutation-inversion isomers. The lowest energy structure of a binary cluster is ultimately determined by several competing effects such as the relative bond strengths of the atom types, size and surface tension mismatches, or energetic penalties due to deviations from equilibrium interatomic distances.[17] Nanocluster structures are often different from those that characterise the corresponding bulk metals and alloys, and can exhibit geometric morphologies that are prohibited by crystallographic translational-symmetry rules such as icosahedral and decahedral motifs with fivefold symmetry axes.[28]

In this thesis, the binary Lennard-Jones (LJ) potential[29] has been chosen to study finite-system analogues of solid-solid phase transitions in binary nanoclusters. Solid-solid transitions of homogeneous LJ systems have been described in detail[30–41] (see Section 1.2.2), but the solid-solid transitions of binary systems are not well documented or understood for LJ or higher levels of theory. This study aims to provide initial results that can be extended to more intricate theoretical models and physical systems.

1.2 The LJ potential

The model for the pair potential between two atoms i and j proposed by Gustav Mie in 1903[42] is

$$\Phi_{ij}(r_{ij}) = \left(\frac{n}{n-m}\right)\left(\frac{n}{m}\right)^{m/(n-m)} \varepsilon \left[\left(\frac{\sigma}{r_{ij}}\right)^{n} - \left(\frac{\sigma}{r_{ij}}\right)^{m}\right], \tag{1.1}$$

where r_{ij} is the distance between atoms i and j, n and m are constants, ε is the pair well depth and σ is the equilibrium pair separation. The Lennard-Jones model[29] is an evaluation of the Mie potential at $n = 12$ and $m = 6$. The total Lennard-Jones potential V_{LJ} for a system of identical atoms is given by Equation (1.2), where $2^{1/6}\sigma$ is the equilibrium pair separation:

$$V_{LJ} = 4\varepsilon \sum_{i<j} \left[\left(\frac{\sigma}{r_{ij}}\right)^{12} - \left(\frac{\sigma}{r_{ij}}\right)^{6}\right]. \tag{1.2}$$

The LJ potential remains in widespread use today due to its mathematical simplic-

ity and computational amenability. The LJ potential was utilised in computational investigations as early as 1954 by Rosenbluth and Rosenbluth[43] for two-dimensional systems during the development of the Monte Carlo method.[44] Three-dimensional systems of atoms interacting in pairs according to the LJ potential were later reported by Wood and Parker for $N = 32$ and 108 atoms.[45] As computational power and global optimisation algorithms improved, likely candidates for the global minima of LJ_N clusters through $N = 309$ were identified by many different groups over nearly three decades.[31,46–65] It was found that most small ($N \lesssim 100$) LJ clusters have global minimum geometries based on Mackay[66] icosahedra.[31,50,54] Some important exceptions exist where LJ clusters have global minima that are not icosahedral. The global minimum of LJ_{38} is a truncated octahedron with face-centred cubic (fcc) packing;[57,58] the global minima of LJ_{75-77} and $LJ_{102-104}$ are based on Marks'[67] decahedra;[58,59] and the global minimum of LJ_{98} is a Leary tetrahedron.[65]

1.2.1 Melting of LJ clusters

Early research on small LJ clusters sought to calculate minimum energy structures, i.e. the structures stable at absolute zero.[68,69] Subsequent studies used molecular dynamics (MD)[70–73] and Monte Carlo[30,74–77] calculations to explore cluster geometries beyond 0 K, which led to the identification of finite-system analogues of solid-liquid and liquid-gas phase transitions. Investigation of phase transitions in small clusters continued,[78–83] though the nature of the solid-liquid transition and the shape of the caloric curve at the transition were not agreed upon. Labastie and Whetten[84] attributed these inconsistencies in predicted properties to differences in the thermodynamic ensembles used to model the clusters. The authors went on to demonstrate that the melting of a cluster can be defined independent of the ensemble considerations using the classical density of states $\Omega(E)$. Subsequent studies[85] used statistical thermodynamics to explore the phase transitions of clusters and construct phase diagrams.

1.2.2 Solid-solid transitions of LJ clusters

The treatment of small LJ clusters with MD and Monte Carlo methods to explore nonzero temperature structures exposed solid-solid transitions prior to melting. Early

evidence of solid-solid transitions was reported by Kaelberer and Etters,[76] who commented briefly on a 'structural transition' between isomeric forms of clusters containing seven or more atoms. Nauchitel and Pertsin further investigated solid-state transitions in their Monte Carlo study,[30] where they demonstrated a change in the free energy global minimum of LJ_{55} from icosahedral to fcc by decreasing the average radial density of the system. Since the potential energy global minimum structure remained the icosahedral version of LJ_{55}, Nauchitel attributed the change in the free energy global minimum to entropic effects. Later,[31] Wales and Doye expanded upon the free energy/potential energy global minimum discrepancy when they noted computational difficulty in locating rare non-icosahedral global minimum structures. Wales attributed this difficulty to the fact that the free energy global minima of these exceptional clusters correspond to the potential energy global minima only at low temperatures well below the melting point. One such cluster is LJ_{38}, which undergoes a solid-solid transition from its fcc global minimum to an incomplete icosahedral structure at approximately two-thirds of the melting temperature.[32,33,41]

Developments in Monte Carlo methods, especially the parallel tempering technique,[86–88] improved the sampling of larger regions of phase space, thereby facilitating further study of solid-solid transitions in small clusters such as LJ_{31},[34,37] LJ_{38},[35,36,38,39] and LJ_{75}.[40] The advantage of these computionally demanding methods was assessed by Sharapov and Mandelshtam,[41] who compared heat capacity results generated from sophisticated Monte Carlo methods with results from alternative calculations using the harmonic superposition approximation (HSA),[68,89–92] which involves a much simpler analysis (see Section 2.1). Sharapov and Mandelshtam concluded that the less intricate HSA approach provides an accurate estimate for the heat capacity around the low-temperature solid-solid transitions of small clusters.

1.2.3 Binary LJ clusters

The LJ model can be expanded to describe binary systems, i.e. systems with two atom types, by Equation (1.3), where α and β are the atom types of atoms i and j, respectively, and $(\alpha, \beta) \in (A, B)$. As with homogeneous LJ systems, binary LJ systems were studied using both Monte Carlo[93–95] and MD[96] methods, or a combination of both.[97,98] Later work[99–103] used more advanced Monte Carlo techniques, such as

parallel tempering or jump-walking.[104]

$$V_{BLJ} = 4\sum_{i<j} \varepsilon_{\alpha\beta} \left[\left(\frac{\sigma_{\alpha\beta}}{r_{ij}} \right)^{12} - \left(\frac{\sigma_{\alpha\beta}}{r_{ij}} \right)^{6} \right] \tag{1.3}$$

Minimum energy cluster geometries were investigated in the context of the relative size (σ_{BB}/σ_{AA}) and 'stickiness' ($\varepsilon_{BB}/\varepsilon_{AA}$) of the two atom types. Garzón et al.[96] examined 13-atom binary LJ systems and noted that a smaller atom type prefers to occupy the central position of the icosahedral structure; this result was later confirmed by Bytheway and Kepert,[105] Frantz,[99] and Munro et al.[106]

The changes in the phase transitions of binary clusters relative to their homogeneous counterparts were also studied.[14,94,95,99,100,103,107] Lopez and Freeman[95] were the first to report 'anomalies' in the heat capacity curve of some binary systems well below the melting temperature, which they likened to the disordering transitions observed in bulk alloys. These small peaks were later attributed by Frantz[99] to the effects of permutation-inversion isomers. Permutation-inversion isomers were further investigated by Sabo et al.,[101] who demonstrated that by tuning the size and 'stickiness' parameters of binary LJ_7, the lowest total energy structure could be selected from one of three possible geometries. In a subsequent paper,[102] Sabo et al. went on to show that by incorporating selected impurity atoms into LJ_{13}, it is possible to stabilise binary structures characteristic of higher-energy homogeneous configurations. Calvo and Yurtsever[14] showed that binary LJ_{38} clusters with atoms of type $A \approx$ krypton and $B \approx$ xenon further stabilise the octahedral global minimum geometry of homogeneous LJ_{38}, while binary clusters with atom types $A \approx$ argon and $B \approx$ xenon favour polytetrahedral geometries over the octahedral structure.

Both Sabo et al.[103] and Quesada and Moyano[107] observed shifts in phase transition temperatures resulting from the incorporation of a second type of atom into an LJ cluster. Sabo et al. observed that replacing some type A atoms in LJ_{13} with less 'sticky' type B atoms ($\varepsilon_{BB}/\varepsilon_{AA} < 1$) resulted in a decrease in melting temperature relative to that of the homogeneous cluster, and an increase in the temperature of the small solid-solid peak as the number of less 'sticky' impurities increased. Quesada and Moyano investigated the effect of a single impurity on the melting of LJ clusters, reporting that the incorporation of one dopant atom can noticeably decrease the

melting temperature of clusters containing fewer than 100 total atoms.

1.3 Overview

The work presented in this thesis aims to describe and explain how the low temperature solid-solid transitions observed in small atomic clusters, namely LJ_{38} and LJ_{31}, can be manipulated. The exchange of a standard atom for a larger or smaller dopant atom affects the relative stabilities of the low-lying minima, and the solid-solid transition of the new binary cluster correspondingly adjusts to the impurity-induced changes. Trends in the cluster solid-solid transition temperature are monitored by a two-state approximation where each state is defined using appropriate lumping criteria.

Chapter 2 discusses the harmonic superposition approximation (HSA) and two-state approximation utilised in thermodynamic analysis. Chapter 3 describes dopant effects on the solid-solid transition of LJ_{38} between fcc and incomplete icosahedral morphologies in the context of potential energy effects. Chapter 4 describes dopant effects on the solid-solid transition of LJ_{31} between two structures based on the same icosahedral core but with different overlayers, and addresses the utility of the two-state approximation.

The results show that the incorporation of a single impurity into LJ_{38} or LJ_{31}, modelled by adjusting a single parameter in the potential, offers control over the solid-solid transitions present in these clusters. The sensitivity of the preferred geometry to a single dopant provides a theoretical precursor for the structural control of solid-state materials, which is briefly explored in Chapter 5.

2 | Methods

2.1 The harmonic superposition approximation

2.1.1 The superposition approach

Thermodynamic properties such as heat capacity can be inferred from the potential energy surface (PES) of sufficiently low-energy systems using the harmonic superposition approximation (HSA).[68,89–92] The superposition component of the HSA defines the configurational part of the phase space integral in terms of the contribution from the catchment basin of each geometrically distinct local minimum on the PES. The density of states $\Omega(E)$ is written as

$$\Omega(E) = \sum_{\mathrm{a}} \Omega_{\mathrm{a}}(E), \tag{2.1}$$

where Ω_{a} is the density of states for the catchment basin of minimum a. Since the minima are geometrically distinct, Ω_{a} must include a factor n_{a} to account for permutation-inversion isomers.[108,109] For a system with N_{A} atoms of element A, etc., and point group order o_{a}, $n_{\mathrm{a}} = 2N_{\mathrm{A}}!N_{\mathrm{B}}!N_{\mathrm{C}}!\cdots/o_{\mathrm{a}}$.

To determine the contribution of some region $\mathcal{A}$ of configuration space to an observable thermodynamic property, the sum in Equation (2.1) is restricted to the minima only in that region.[110] The probability of finding the system in region $\mathcal{A}$ is given by Equation (2.2) for the microcanonical density of states:

$$P_{\mathcal{A}}(E) = \frac{1}{\Omega(E)} \sum_{\mathrm{a}\in\mathcal{A}} \Omega_{\mathrm{a}}(E). \tag{2.2}$$

2.1.2 The harmonic approximation

In principle, the classical density of states $\Omega(E)$ provides all the information necessary to calculate thermodynamic properties of a system.[108,109] For greater efficiency, the harmonic method approximates the classical density of states in Equation (2.1) as

$$\Omega_{\mathrm{a}}(E) \approx \widetilde{\Omega}_{\mathrm{a}}(E) = \frac{n_{\mathrm{a}}(E - V_{\mathrm{a}})}{\Gamma(\kappa)(h\overline{\nu}_{\mathrm{a}})^{\kappa}}. \tag{2.3}$$

For a system with N particles and $3N - 6 = \kappa$ degrees of freedom, $\widetilde{\Omega}(E) = \sum_{V_{\mathrm{a}}<E} \widetilde{\Omega}_{\mathrm{a}}$, where each geometrically distinct minimum a has potential energy $V_{\mathrm{a}} < E$ and geometric mean vibrational frequency $\overline{\nu}_{\mathrm{a}}$. The symmetry factor n_{a} is the same as in Section 2.1.1, h is Planck's constant and $1/h^{\kappa}$ is included to maintain agreement with the classical limit of quantum statistical mechanics.[108,109] Taking the Laplace transform of $\widetilde{\Omega}$ with respect to E yields an approximation to the vibrational partition function $Z_{\mathrm{vib}}(T)$ in the canonical ensemble, where T is the temperature and k_B is the Boltzmann constant:

$$\widetilde{Z}_{\mathrm{vib}}(T) = \sum_{\mathrm{a}} n_{\mathrm{a}} e^{-V_{\mathrm{a}}/k_B T} \left(\frac{k_B T}{h\overline{\nu}_{\mathrm{a}}}\right)^{\kappa}. \tag{2.4}$$

The HSA has been shown to produce useful results at lower temperatures[68,89,108] and continues to be used instead of more complicated methods.[41,111] A full derivation of the harmonic approximation (i.e. Equations (2.3) and (2.4)) is provided in Appendix A.

2.1.3 Thermodynamic properties

The average total energy for the canonical ensemble under the HSA is given by

$$\langle E \rangle = \kappa k_B T + \frac{1}{\widetilde{Z}_{\mathrm{vib}}(T)} \sum_{\mathrm{a}} \frac{n_{\mathrm{a}} e^{-V_{\mathrm{a}}/k_B T} V_{\mathrm{a}}}{(h\overline{\nu}_{\mathrm{a}}/k_B T)^{\kappa}}. \tag{2.5}$$

$(\partial\langle E\rangle/\partial T)_V$ gives the constant volume heat capacity, which is useful for the detection of phase transitions. The heat capacity for the canonical ensemble at constant volume is thus obtained from Equation (2.5):

$$C(T)_{\mathrm{vib}} = \kappa k_B - \frac{\widetilde{Z}_{1,\mathrm{vib}}(T)^2}{k_B T^2 \widetilde{Z}_{0,\mathrm{vib}}(T)^2} + \frac{\widetilde{Z}_{2,\mathrm{vib}}(T)}{k_B T^2 \widetilde{Z}_{0,\mathrm{vib}}(T)}, \tag{2.6}$$

where

$$\widetilde{Z}_{p,\mathrm{vib}}(T) = \sum_{\mathrm{a}} n_{\mathrm{a}} (V_{\mathrm{a}})^p e^{-V_{\mathrm{a}}/k_B T} \left(\frac{k_B T}{h\overline{\nu}_{\mathrm{a}}} \right)^{\kappa}. \tag{2.7}$$

Features of interest, such as the solid-solid transition temperature (T_{ss}) of a system, can be identified by inspection of the heat capacity curve generated from Equation (2.6). T_{ss} can also be calculated numerically by adapting Equation (2.4) to describe the free energy of a given solid state. Under the HSA, the local (Helmholtz) free energy of minimum i is defined as

$$f_i(T) = -k_B T \ln \widetilde{z}_i(T) = V_i + k_B T \ln o_i \bar{\nu}_i^{\kappa} + h(T), \tag{2.8}$$

where $\widetilde{z}_i$ is the contribution of minimum i to the (vibrational) canonical partition function, V_i is the potential energy of minimum i, o_i is the point group order, $\bar{\nu}_i$ is the geometric mean vibrational frequency, $3N - 6 = \kappa$ is the number of vibrational degrees of freedom and $h(T)$ is a temperature dependent function that is independent of i.

To extend Equation (2.8) from a single minimum i to a set of minima α associated with a particular state or phase, the partition functions for all minima $i \in \alpha$ must be summed:

$$\widetilde{Z}_{\alpha}(T) = \sum_{i \in \alpha} \widetilde{z}_i(T). \tag{2.9}$$

The corresponding lumped free energy[112] for α can be written as

$$F_{\alpha}(T) = -k_B T \ln \widetilde{Z}_{\alpha}(T) = V_{m_\alpha} + k_B T \ln \frac{o_{m_\alpha} \bar{\nu}_{m_\alpha}^{\kappa}}{1 + \zeta_{\alpha}(T)} + H(T), \tag{2.10}$$

where $\widetilde{Z}_{\alpha}$ represents the statistical weight of α (its lumped partition function), m_α identifies the lowest-energy minimum in α, and

$$\zeta_{\alpha} = \sum_{i \in \alpha \setminus m_\alpha} \widetilde{z}_i(T) / \widetilde{z}_{m_\alpha}(T). \tag{2.11}$$

If there is a thermally-driven transition between two distinct solid states α and β, then the corresponding lumped local free energies will be equal at the transition temperature T_{ss}. In other words, T_{ss} is identified by

$$F_\alpha - F_\beta = V_{m_\alpha} - V_{m_\beta} + k_B T_{\mathrm{ss}} \ln \left[\frac{o_{m_\alpha} \bar{\nu}_{m_\alpha}^{\kappa}}{o_{m_\beta} \bar{\nu}_{m_\beta}^{\kappa}} \frac{1 + \zeta_\beta(T_{\mathrm{ss}})}{1 + \zeta_\alpha(T_{\mathrm{ss}})} \right] = 0. \tag{2.12}$$

Since Equation (2.12) is not analytically straightforward, T_{ss} is calculated numerically by locating the root of $F_\alpha - F_\beta$. If a positive solution to Equation (2.12) does not exist, this result indicates the absence of a thermally-driven transition between α and β.

2.2 Minima databases

The HSA requires a representative sample of local minima from which the potential energies, vibrational frequencies, and point group orders can be inferred. The global minimum and other low-lying minima are necessary for accurate analysis because they are weighted heavily in the partition function (see Equation (2.4)). In the limit of zero temperature, the global minimum dictates all thermodynamics, and it remains particularly important at low temperatures. The absence of any one low-lying minimum can affect the accuracy of properties generated from $\widetilde{Z}$, such as the heat capacity curve and phase transition temperatures.

In the present study, two different protocols based on the basin-hopping algorithm[31,109] were used for global optimisation of binary LJ systems. Initial databases of minima for LJ_{38} and LJ_{31} were determined for each homogeneous cluster using basin-hopping. Heat capacity curves for LJ_{38} were found to converge using a database containing approximately 1000 minima, so the 1000 lowest homogeneous minima of the relevant system were chosen for analysis (except where otherwise noted). To produce the first type of database for corresponding binary LJ systems, the permutation-inversion isomers of the previously identified 1000 lowest minima were enumerated for each set of LJ parameters, which yielded about 35,000 minima for each binary LJ_{38} system and 28,000 minima for each binary LJ_{31} system. A second type of database for each binary system was generated by performing global optimisation on binary

structures using basin-hopping.

The exhaustive enumeration of permutation-inversion isomers of the homogeneous minima (first protocol) yielded results consistent with the use of similarly-sized databases generated by performing global optimisation on binary structures from the outset (second protocol). This consistency check provides evidence that all important, low-lying minima are found in both types of databases. The exhaustive approach was selected for analysis of binary LJ clusters because of its firmer connection to the homogeneous system.

3 | LJ_{38}

The 38-atom Lennard-Jones cluster (LJ_{38}) features an fcc global minimum and undergoes a solid-solid transition to an incomplete icosahedral structure before melting. This solid-solid transition is sensitive to the relative stabilities of the low-lying minima. A single atom in the LJ_{38} cluster can be exchanged for a new atom ($N_A = 1$, $N_B = 37$) that differs from the B atoms only in the value of its size parameter (σ_{AB}). The incorporation of a larger or smaller dopant into the cluster changes the energies of the minima and systematically affects the solid-solid transition. By choosing small perturbations in the dopant size parameter, a decrease in the solid-solid transition temperature of LJ_{38} can be attained.

3.1 The solid-solid transition

LJ_{38} is characterised by a double-funnel energy landscape, where the fcc global minimum has a different morphology from the other low-lying minima, which are based on incomplete icosahedra (Figure 3.1).[32,33,113,114] The global minimum of LJ_{38} is a truncated octahedron (point group O_h) with fcc packing.[57,58] This structure is uncommon among small LJ clusters, most of which have global minima based on Mackay[66] icosahedra.[31,50,54] The LJ_{38} cluster undergoes a solid-solid transition from the fcc to the incomplete icosahedral geometry, which manifests as a feature in the heat capacity preceding the more pronounced melting peak (Figure 3.2).[32,35,36,41,111,113,114] Previous studies[32,33,41] have reported a transition temperature of $k_B T_{ss}/\varepsilon \approx 0.12$, which corresponds to about 14 K using the Rowley, Nicholson and Parsonage parameter set for argon.[115]

The temperature of the LJ_{38} solid-solid transition between the fcc and icosahedral states was calculated by Equation (2.12) to be $k_B T_{ss}/\varepsilon = 0.120$ using a database of

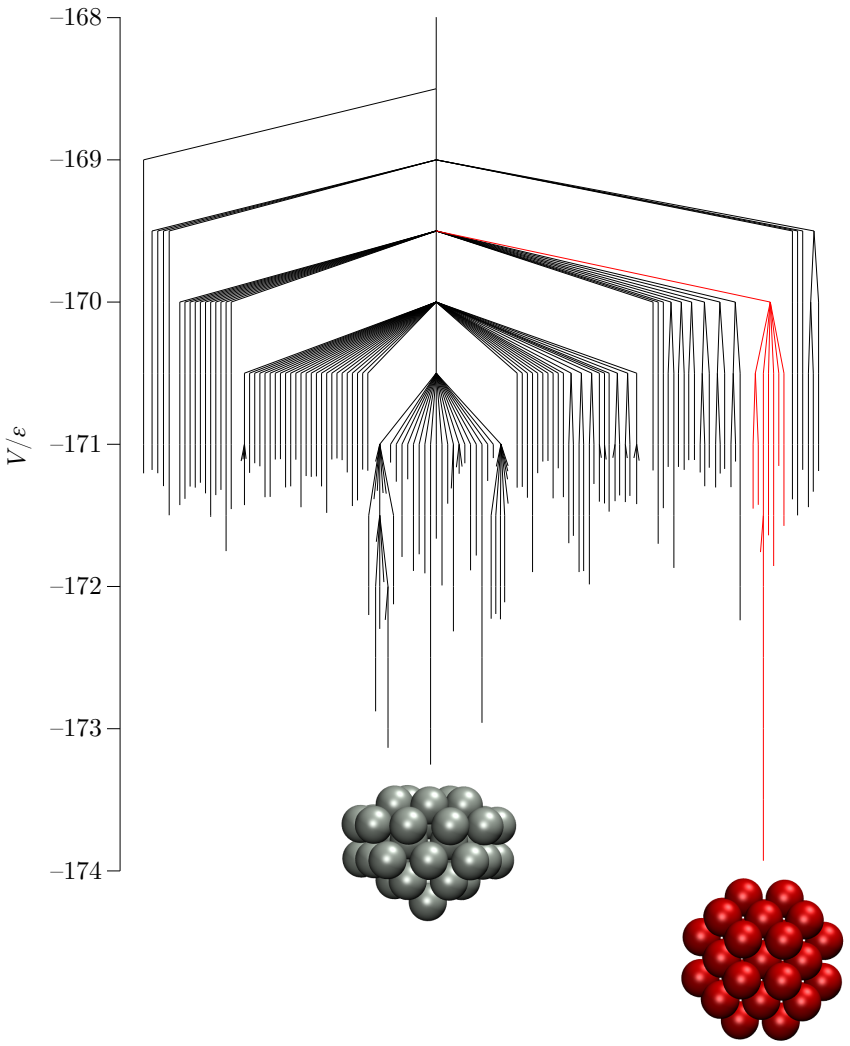

Figure 3.1: A disconnectivity graph[116,117] for representative minima of the homogeneous LJ_{38} cluster.[118] A disconnectivity graph shows which minima are connected using pathways that lie below a series of energy thresholds.[118] The lowest energy minima corresponding to the icosahedral (grey) and fcc (red) funnels are shown.

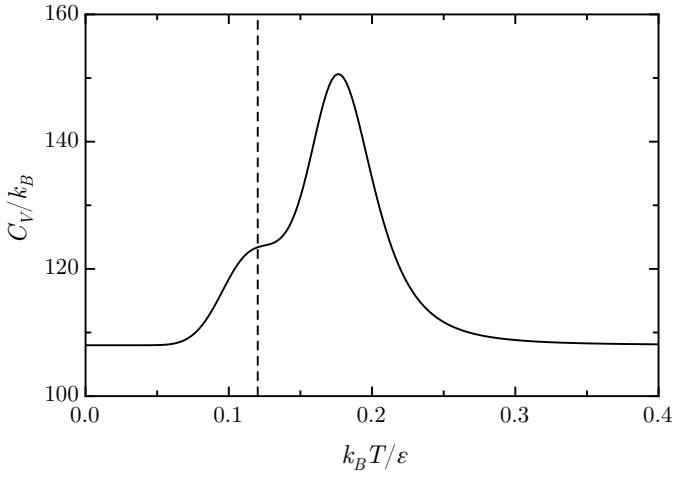

Figure 3.2: Constant volume heat capacity for homogeneous LJ_{38}. The larger peak at $k_BT/\varepsilon \approx 0.18$ represents the melting transition and the smaller shoulder represents the solid-solid transition. The dotted line at $k_BT/\varepsilon = 0.120$ indicates T_{ss} according to Equation (2.12).

the 1000 lowest minima of homogeneous LJ_{38} (see Section 2.2). The global minimum was chosen as the only minimum to represent the fcc state, and the remaining 999 minima contributed to the icosahedral state.[a]

3.2 Dopant effects on the solid-solid transition

In the present analysis a standard atom in the LJ_{38} cluster is exchanged for a single impurity ($N_A = 1$, $N_B = 37$) that differs only in its relative size (σ_{AB} is varied; $\sigma_{AA} = \sigma_{BB} = 1$; $\varepsilon_{AA} = \varepsilon_{AB} = \varepsilon_{BB} = 1$). Only small changes in dopant size are considered ($0.95 \leq \sigma_{AB} \leq 1.05$) because dopant atoms with greater size differences perturb the geometries of the homogeneous minima significantly, such that the lowest-lying binary minima no longer resemble the lowest-lying homogeneous minima. T_{ss} was calculated for the binary clusters as described in Section 3.1 for homogeneous LJ_{38} using permutation-inversion isomers generated from the database of homogeneous minima (see Section 2.2). The results show that the incorporation of a dopant atom into LJ_{38} offers a tunable decrease of the solid-solid transition temperature between the fcc and higher-energy icosahedral structures within the regions where the fcc structure remains the global minimum ($0.98 \lesssim \sigma_{AB} \leq 1.05$) (Figure 3.3). For $0.95 \leq \sigma_{AB} \lesssim 0.98$, an incomplete icosahedral geometry becomes the global minimum and there is no signature of a solid-solid transition in the heat capacity before melting.

3.2.1 Vibrational entropy contribution

T_{ss} depends on the free energies of the fcc and icosahedral states of the LJ_{38} system (see Equation (2.12)). For a given minimum i, the potential energy V_i and an entropic contribution determine the free energy (Equation (2.8)). The entropic contribution to the free energy F_α in Equation (2.10) from a single minimum $i \in \alpha$ is $k_B T \ln o_i \bar{\nu}_i^\kappa$, where the point group order o_i encodes the landscape entropy and $\bar{\nu}_i$, which represents the basin entropy, is the geometric mean vibrational frequency of minimum i for $3N - 6 = \kappa$ vibrational degrees of freedom.[109] For this analysis the translational and rotational contributions were shown to be unimportant and are systematically

[a]The use of an order parameter to distinguish higher energy minima that might belong in the fcc funnel was investigated, but produced no significant change in the result. All 1000 minima were used to generate T_{ss}, but only the 9 lowest minima are required to achieve accuracy to three significant figures.

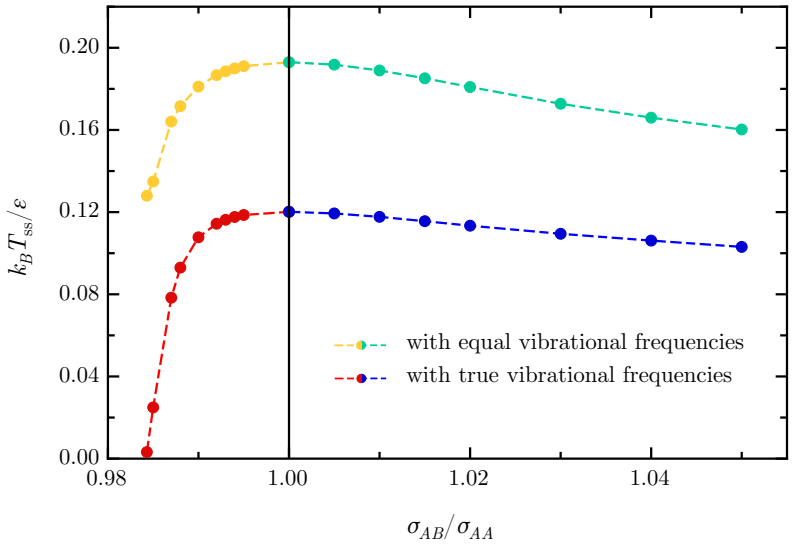

Figure 3.3: The solid-solid transition temperature of LJ_{38} as a function of the dopant size parameter σ_{AB}. The red and blue curve shows the true results, and the yellow and green curve shows the results when the vibrational frequencies are set to a constant value. For $\sigma_{AB} < 1.00$ (yellow and red), the lowest-lying structures feature the dopant atom on the interior of the cluster. For $\sigma_{AB} > 1.00$ (green and blue), the lowest-lying structures feature the dopant atom on the exterior of the cluster.

neglected.

To assess the effect of the basin entropy on the free energies that determine T_{ss}, all values of T_{ss} were recalculated without the vibrational contributions. This analysis was achieved by replacing the actual value of $\ln \bar{\nu}_i^{\kappa}$ with a nonzero constant before calculating the lumped partition functions for states $\alpha \equiv$ fcc and $\beta \equiv$ icos (Equation (2.9)) and solving Equation (2.12) for T_{ss}. The point group order o_i, which corresponds to the landscape entropy, was retained in this analysis.[b]

The original and basin entropy controlled results are presented in Figure 3.3, which shows that removing the basin entropy component from the analysis results in an offset of the T_{ss} values, but does not change the shape of the curve. The positive offset occurs because the less stable icosahedral structures have softer modes (lower $\ln \bar{\nu}_i^{\kappa}$) than the fcc structures.[32,33,35,36] When the vibrational frequencies are set to a constant, a higher temperature is needed to stabilise the icosahedral structures because the entropic favourability of the transition is reduced. Since the T_{ss} curve shape does not depend on the vibrational frequency component of F_{α}, conclusions drawn from potential energy alone dominate the overall free energy analysis.

[b]Setting all the point group orders equal to 1 produces a small, positive offset of the true curve in Figure 3.3.

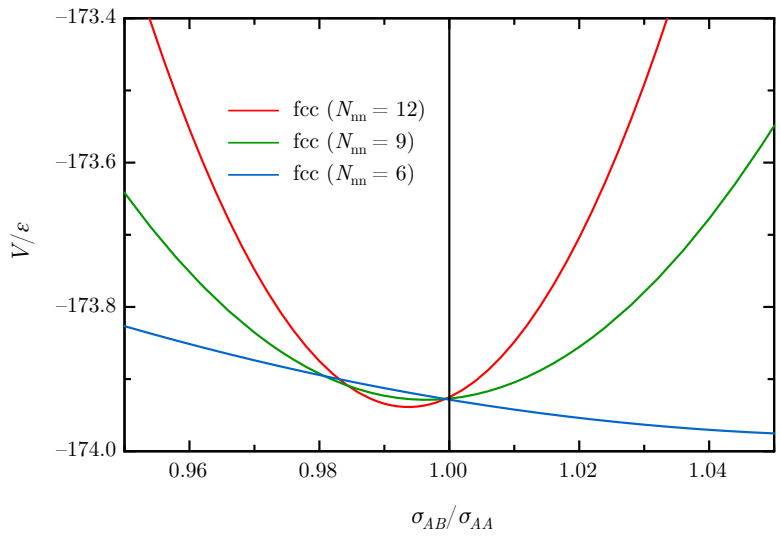

Figure 3.4: The potential energy V of the three permutation-inversion isomers of $LJ_{38}^{(1)}$ for dopant size parameters $0.95 \leq \sigma_{AB} \leq 1.05$, where $\sigma_{AB} = 1.00$ represents the homogeneous structure.

3.3 Potential energy analysis

3.3.1 Nearest neighbour effects

The introduction of a dopant atom into LJ_{38} affects the relative energies of minima in the fcc and icosahedral funnels, and it has been demonstrated in Section 3.2.1 that this relationship determines T_{ss} (see Equation (2.12)). The low-lying minima energies are impacted in different ways depending on the local environment of the dopant atom, which is characterised by the number and arrangement of atoms surrounding the dopant. For the octahedral global minimum of homogeneous LJ_{38} ($LJ_{38}^{(1)}$), every atom is located within an fcc packing environment. There are three unique dopant positions, which differ only in the number of neighbours, N_{nn}, within a threshold distance of the dopant atom. Figure 3.4 shows the potential energies of the three binary $LJ_{38}^{(1)}$ structures.

The potential energy of a binary $LJ_{38}^{(1)}$ minimum is more sensitive to the size of the dopant atom when N_{nn} is larger. This trend in sensitivity results from the effect of the dopant atom on the distances of its nearest neighbours. When the size of a dopant atom causes a nearest neighbour distance to deviate from the equilibrium pair distance, an energetic penalty V_{strain} is incurred.[119,120] In an fcc dopant environment, V_{strain} for a given dopant size increases as N_{nn} increases, so the fcc structures with

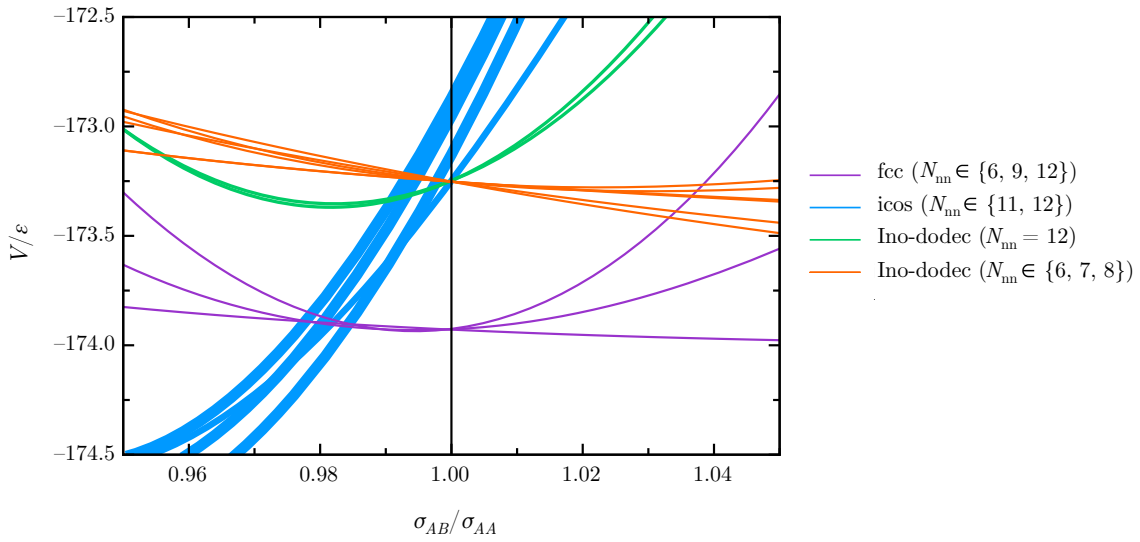

Figure 3.5: The potential energy V of the lowest-lying minima of binary LJ_{38} for dopant size parameters $0.95 \leq \sigma_{AB} \leq 1.05$. Different dopant packing environments are indicated with different colours on the graph, and the thickness of each curve is proportional to $\exp(V_{\text{strain}})$ at $\sigma_{AB} = 1.00$ for that minimum. $\sigma_{AB} = 1.00$ represents the homogeneous structure, where the energies of the possible doped isomers of the same homogeneous minimum $LJ_{38}^{(i)}$ are the same.

higher N_{nn} are more destabilised by the presence of a dopant atom. V_{strain} calculations for the three fcc environments of $LJ_{38}^{(1)}$ are presented in Appendix B.

3.3.2 Local packing effects

The arrangement of atoms surrounding the dopant also affects the stability of a given binary structure as a function of dopant size. The octahedral global minimum of the homogeneous system $LJ_{38}^{(1)}$ features all its constituent atoms within fcc-type packing environments. The other low-lying minima (namely $LJ_{38}^{(2-5)}$) are based on incomplete icosahedral geometries and offer dopant locations within either icosahedral or Ino-dodecahedral packing environments with varying N_{nn}. An icosahedral packing environment can be described by two staggered five-membered rings of neighbours plus two additional neighbours on either side of the dopant on the axis orthogonal to the (parallel) planes of the two rings. An Ino-dodecahedral environment is similar to the icosahedral environment, except that the two five-membered rings are eclipsed as opposed to staggered, creating a more loosely-packed structure.[c]

Each homogeneous structure among $LJ_{38}^{(2-5)}$ contains one dopant atom location that features icosahedral packing, and these locations have complete ($N_{\text{nn}} = 12$,

[c] Compare Figures 3.6d and 3.6f.

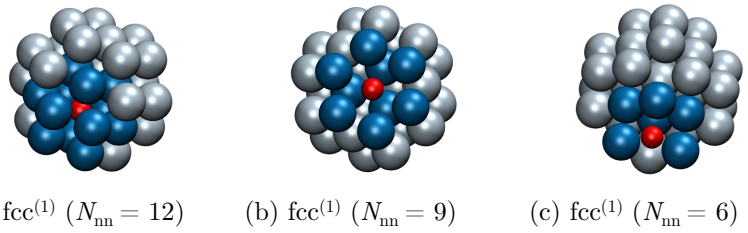

(a) fcc$^{(1)}$ ($N_{\mathrm{nn}} = 12$) (b) fcc$^{(1)}$ ($N_{\mathrm{nn}} = 9$) (c) fcc$^{(1)}$ ($N_{\mathrm{nn}} = 6$)

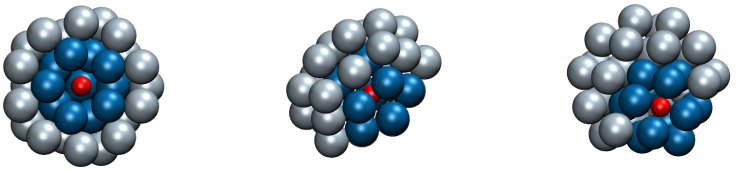

(d) icos$^{(2)}$ ($N_{\mathrm{nn}} = 11$) (e) Ino-dd$^{(2)}$ ($N_{\mathrm{nn}} = 12$) (f) Ino-dd$^{(2)}$ ($N_{\mathrm{nn}} = 12$)

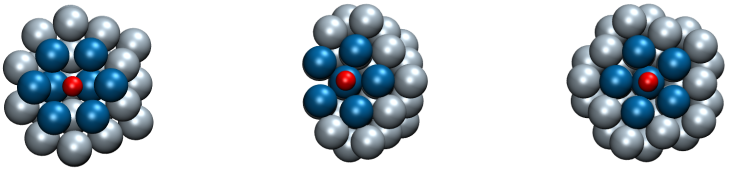

(g) Ino-dd$^{(2)}$ ($N_{\mathrm{nn}} = 8$) (h) Ino-dd$^{(2)}$ ($N_{\mathrm{nn}} = 6$) (i) Ino-dd$^{(2)}$ ($N_{\mathrm{nn}} = 6$)

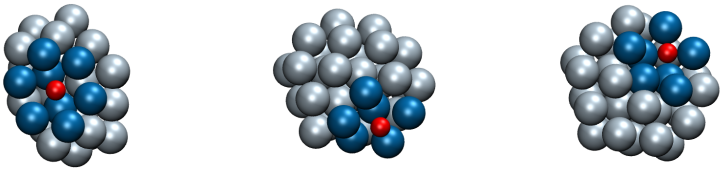

(j) Ino-dd$^{(2)}$ ($N_{\mathrm{nn}} = 8$) (k) Ino-dd$^{(2)}$ ($N_{\mathrm{nn}} = 6$) (l) Ino-dd$^{(2)}$ ($N_{\mathrm{nn}} = 7$)

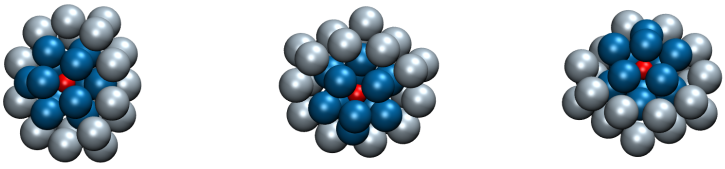

(m) icos$^{(3)}$ ($N_{\mathrm{nn}} = 12$) (n) icos$^{(4)}$ ($N_{\mathrm{nn}} = 12$) (o) icos$^{(5)}$ ($N_{\mathrm{nn}} = 12$)

Figure 3.6: The structures and environments of low-lying binary minima from $\mathrm{LJ}_{38}^{(1-5)}$. The nearest neighbours of the dopant are coloured blue and the dopant atom is coloured red. Superscripts (1) through (5) indicate from which homogeneous minimum each binary structure is derived and 'Ino-dd' signifies an Ino-dodecahedral packing environment. All three unique structures of binary $\mathrm{LJ}_{38}^{(1)}$ (a-c) and all nine unique structures of binary $\mathrm{LJ}_{38}^{(2)}$ (d-l) are shown, as well as the structure from each of binary $\mathrm{LJ}_{38}^{(3-5)}$ that features icosahedral packing of the dopant atom (m-o).

$LJ_{38}^{(3-5)}$) or nearly complete ($N_{nn} = 11$, $LJ_{38}^{(2)}$) neighbour shells. The remaining dopant positions are located within Ino-dodecahedral packing environments with $N_{nn} \in \{6, 7, 8, 12\}$.[d] Dopants within icosahedral packing environments induce the highest V_{strain} (see Appendix B), so binary structures that feature icosahedral local packing of the dopant atom are the most sensitive to changes in the dopant size and are generally stabilised by the presence of a smaller dopant. This is the expected result, since the radial distance inside an icosahedron is about 5% less than the nearest neighbour distance for atoms on the surface, which feature Ino-dodecahedral packing environments.[13] Structures with Ino-dodecahedral dopant packing environments are generally destabilised by the incorporation of a dopant, although the presence of a larger dopant atom can slightly stabilise structures with incomplete neighbour shells, i.e. $N_{nn} \in \{6, 7, 8\}$. An illustration of how different dopant packing environments and strain energies affect the potential energies of the binary structures for both larger and smaller dopants is provided in Figure 3.5. Figure 3.6 shows the structures and environments of the low-lying minima from $LJ_{38}^{(1-5)}$.

3.4 Discussion

The exchange of a standard LJ_{38} atom for a dopant atom of a different size changes the energies of the minima, which affect T_{ss}. Larger dopant atoms prefer locations on the cluster exterior, while smaller dopant atoms generally prefer interior locations. Doping with a larger atom and with a smaller atom therefore involve different sets of low-lying minima and are analysed separately.

3.4.1 Doping with one larger atom

Due to the number and arrangement of neighbours around the dopant atom, changes in the heat capacity profile of LJ_{38} are induced by changing the size of the dopant incorporated into the system. When exchanging one standard atom for a larger dopant atom, for small changes in dopant size ($1.00 < \sigma_{AB} \leq 1.05$) the dopant prefers locations with a minimum number of neighbours in order to reduce V_{strain} for the larger

[d] Two dopant positions are located within six-neighbour environments wherein the packing cannot be definitively described as either icosahedral or Ino-dodecahedral because only one five-member ring is present (Figure 3.6h,i). Such environments will be classified as Ino-dodecahedral for succinctness.

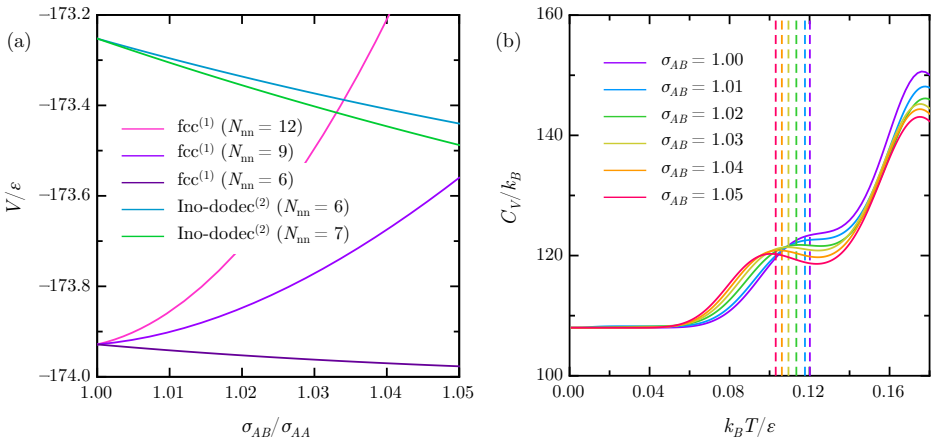

Figure 3.7: (a) The potential energy V of the lowest-lying minima of binary LJ_{38} for dopant radii $\sigma_{AB} > 1.00$. The set of minima shown is representative as opposed to complete. Superscripts (1) and (2) indicate from which homogeneous minimum each binary structure is derived. $\sigma_{AB} = 1.00$ represents the homogeneous structure, where the energies of the possible doped isomers of the same homogeneous minimum $LJ_{38}^{(i)}$ are the same. (b) The heat capacity of binary LJ_{38} for incrementally increasing values of σ_{AB} from 1.00 to 1.05. The solid-solid transition temperature shifts to the left as σ_{AB} increases. The dotted lines range from $k_BT/\varepsilon = 0.120$ (violet, $\sigma_{AB} = 1.00$) to 0.103 (red, $\sigma_{AB} = 1.05$) and indicate k_BT_{ss}/ε for a given σ_{AB} value according to Equation (2.12). The prominent feature near $k_BT/\varepsilon \approx 0.18$ is the melting peak.

impurity. In the fcc funnel, the dopant atom prefers to be located on the edge of the truncated octahedron ($N_{nn} = 6$) (Figure 3.6c). In the icosahedral funnel, the lowest-energy structures feature the dopant within an incomplete Ino-dodecahedral environment ($N_{nn} \in \{6, 7, 8\}$) (Figure 3.6g-l).

For the dopant size range investigated, one fcc structure is slightly stabilised as the size of the dopant increases, but the rest are destabilised. The icosahedral structures featuring incomplete shell Ino-dodecahedral dopant packing environments are stabilised to a greater extent, but the global minimum is unchanged (Figure 3.7a). As the energy difference between the lowest-lying fcc and icosahedral structures decreases, T_{ss} also decreases (see Equation 2.12). The incorporation of an increasingly large dopant atom into LJ_{38} thereby offers a tunable decrease of the cluster solid-solid transition temperature. The heat capacity curves resulting from incrementally larger values of σ_{AB} are illustrated in Figure 3.7b.

3.4.2 Doping with one smaller atom

With small decreases in dopant size ($0.95 \leq \sigma_{AB} < 1.00$), for structures in the fcc funnel the dopant prefers the location with the fewest neighbours ($N_{nn} = 6$) (Figure 3.6c), as for a larger dopant. In the icosahedral funnel, the dopant prefers icosahedral lo-

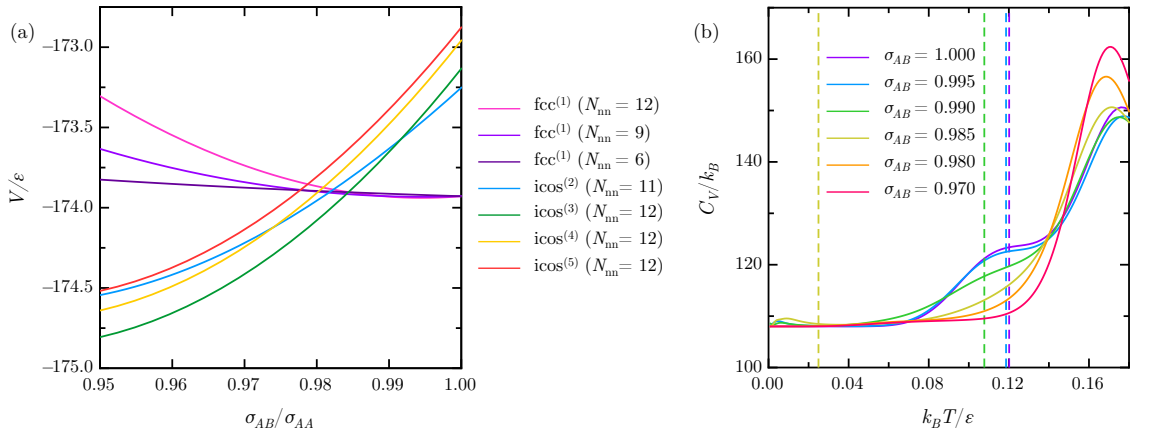

Figure 3.8: (a) The potential energy V of the lowest-lying minima of binary LJ_{38} for dopant radii $\sigma_{AB} < 1.00$. The set of minima shown is representative as opposed to complete. Superscripts (1) through (5) indicate from which homogeneous minimum each binary structure is derived. $\sigma_{AB} = 1.00$ represents the homogeneous structure, where the energies of the possible doped isomers of the same homogeneous minimum $LJ_{38}^{(i)}$ are the same. (b) The heat capacity of binary LJ_{38} for decreasing values of σ_{AB} from 1.00 to 0.97. The solid-solid transition shoulder remains for σ_{AB} close to 1.00 but disappears for $\sigma_{AB} \leq 0.98$. The dotted lines range from $k_BT/\varepsilon = 0.120$ (violet, $\sigma_{AB} = 1.00$) to 0.025 (gold, $\sigma_{AB} = 0.985$) and indicate $k_BT_{\rm ss}/\varepsilon$ for a given σ_{AB} value according to Equation (2.12). The small feature near $k_BT/\varepsilon = 0$ is a permutation-inversion isomerisation peak (see Section 3.4.3) and the prominent feature near $k_BT/\varepsilon \approx 0.18$ is the melting peak.

cal packing environments, which have complete or nearly complete neighbour shells ($N_{\rm nn} \in \{11, 12\}$) (Figure 3.6d,m-o). For the dopant size range examined, the lowest energy fcc structure is destabilised as σ_{AB} decreases, while the low-lying icosahedral structures are significantly stabilised (Figure 3.8a). At $\sigma_{AB} \approx 0.984$, an incomplete icosahedral structure (binary $LJ_{38}^{(3)}$) becomes the global minimum of the system.

While the fcc structure remains the global minimum ($0.984 < \sigma_{AB} \leq 1.000$), the solid-solid transition temperature is shown to decrease (Figure 3.8b). Once the global minimum becomes icosahedral ($0.950 \leq \sigma_{AB} \lesssim 0.984$), a solid-solid transition does not produce a significant heat capacity feature. Compared to the use of a larger dopant, the incorporation of a smaller atom offers a shorter σ_{AB} range on which $T_{\rm ss}$ can be tuned. However, introducing a dopant atom with a sufficiently small size parameter ($\sigma_{AB} \lesssim 0.984$) affords control over the LJ_{38} global minimum structure, which switches from an fcc truncated octahedron to an incomplete icosahedron.

3.4.3 Low temperature permutation-inversion isomerisations

Upon the incorporation of a dopant atom with size parameter $\sigma_{AB} \neq 1.00$, a small feature appears in the heat capacity at very low temperatures ($k_BT/\varepsilon \lesssim 0.005$).

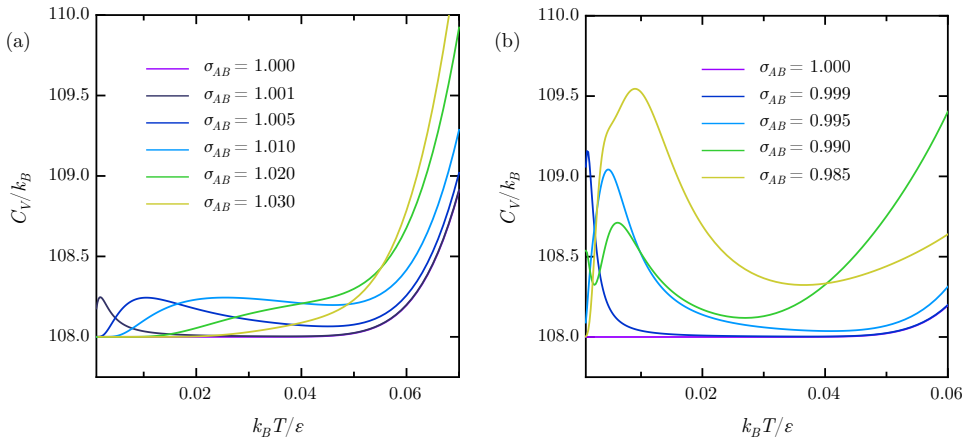

Figure 3.9: (a) The heat capacity of binary LJ_{38} for increasing values of σ_{AB} from 1.00 to 1.03. The small peak at low temperatures represents a transition between permutation-inversion isomers of $LJ_{38}^{(1)}$. The more prominent feature around $k_BT/\varepsilon \approx 0.06$ is the beginning of the solid-solid transition between fcc and icosahedral morphologies (see Section 3.4.1). (b) The heat capacity of binary LJ_{38} for decreasing values of σ_{AB} from 1.000 to 0.985. The leftmost peak at low temperatures represents a transition between permutation-inversion isomers of $LJ_{38}^{(1)}$. The permutation-inversion isomerisation peak overlaps with the solid-solid transition peak from fcc to icosahedral morphologies as σ_{AB} approaches 0.984 (see Section 3.4.2).

This peak is present for both larger and smaller dopants, and is visible in Figure 3.8b. This small, low-temperature peak corresponds to permutation-inversion isomerisations among the three different binary $LJ_{38}^{(1)}$ minima. A similar peak remains upon the removal of any one permutation-inversion isomer of $LJ_{38}^{(1)}$, but no peak appears at $k_BT/\varepsilon \lesssim 0.005$ upon the removal of any two isomers.[e] The low-temperature regions of the heat capacity plots in Figures 3.7b and 3.8b are reproduced in Figure 3.9 with curves for representative values of σ_{AB}. Permutation-inversion isomerisations of LJ clusters have been noted for LJ_7[101] and investigated for LJ_{13}.[95,99,100,106,121] To the author's knowledge this is the first report of permutation-inversion isomerisation in the fcc funnel of LJ_{38}.

3.4.4 Increasing the solid-solid transition temperature

Adjusting the size of a single dopant in LJ_{38} produces a tunable decrease of the solid-solid transition temperature within the regions where the fcc morphology remains the global minimum ($0.98 \lesssim \sigma_{AB} \leq 1.05$). However, the incorporation of a dopant atom with varying size has not been found to increase the solid-solid transition temperature

[e] Assigning different combinations of $LJ_{38}^{(1)}$ permutation-inversion isomers to solid states and solving Equation 2.12 for T_{ss} did not consistently produce values in agreement with heat capacity features.

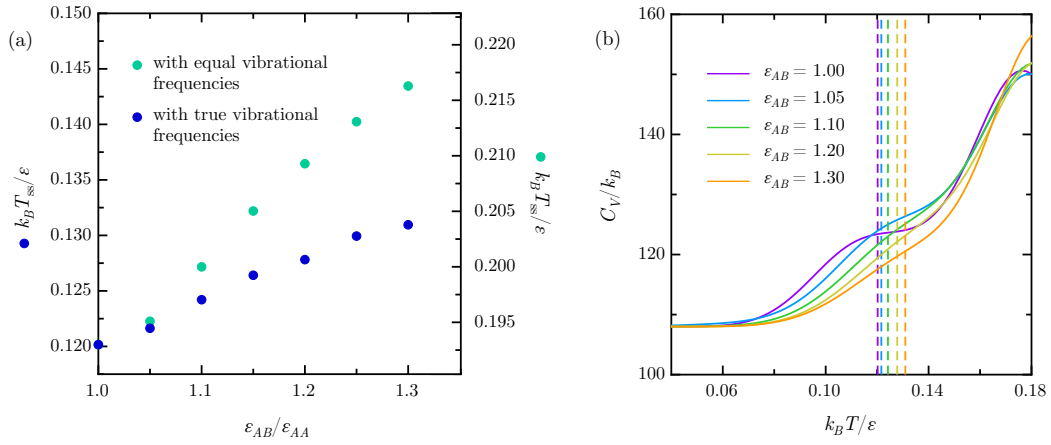

Figure 3.10: (a) The solid-solid transition temperature of LJ_{38} as a function of the 'stickiness' of the dopant atom ε_{AB}. The blue circles show the true results (left axis), and the green circles show the results when the vibrational frequencies are set to a constant value (right axis). The plots are superimposed for comparison. (b) The heat capacity of binary LJ_{38} for increasing values of ε_{AB} from 1.00 to 1.30. The solid-solid transition temperature shifts to the right as ε_{AB} increases. The dotted lines range from $k_BT/\varepsilon = 0.120$ (violet, $\varepsilon_{AB} = 1.00$) to 0.131 (orange, $\varepsilon_{AB} = 1.30$) and indicate k_BT_{ss}/ε for a given ε_{AB} value according to Equation (2.12). The prominent feature near $k_BT/\varepsilon \approx 0.18$ is the melting peak.

of LJ_{38}. Preliminary results that show an increase in the LJ_{38} T_{ss} are presented in order to demonstrate the existence of this type of trend and suggest an avenue for future analysis.

In this investigation, a standard atom in the LJ_{38} cluster is exchanged for a single impurity ($N_A = 1$) that differs only in its 'stickiness' (ε_{AB} is varied; $\varepsilon_{AA} = \varepsilon_{BB} = 1$; $\sigma_{AA} = \sigma_{AB} = \sigma_{BB} = 1$). Increases in dopant 'stickiness' ($\varepsilon_{AB} > 1.00$) are shown to increase the temperature of the LJ_{38} solid-solid transition from fcc to icosahedral. Equation (2.12) was utilised to calculate T_{ss} and heat capacity curves were generated from minima databases analogous to those described in Section 3.2 (Figure 3.10). The basin entropy controlled T_{ss} values were also calculated (as described in Section 3.2.1) and are superimposed with the true values in Figure 3.10a, which show that T_{ss} is more sensitive to increases in ε_{AB} when the vibrational frequencies are held constant.

3.4.5 Preliminary results with an even larger dopant

Incremental increases of the size of a dopant atom from $1.00 \leq \sigma_{AB} \leq 1.05$ offer a tunable decrease of the LJ_{38} solid-solid transition temperature (recall Section 3.4.1). A dopant atom with size parameter $\sigma_{AB} > 1.05$ is large enough to significantly perturb the homogeneous minima geometries from which each binary minimum is derived, such

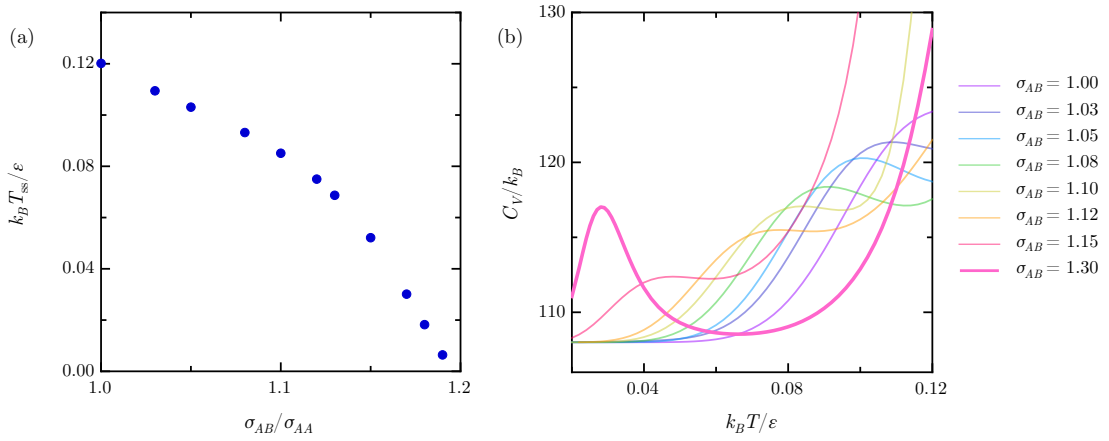

Figure 3.11: (a) The solid-solid transition temperature of LJ_{38} as a function of the size of the dopant atom σ_{AB}. (b) The heat capacity of binary LJ_{38} for increasing values of σ_{AB} from 1.00 to 1.30. The solid-solid transition shoulder shifts towards $k_BT/\varepsilon = 0$ as σ_{AB} approaches 1.20. For $\sigma_{AB} > 1.20$, e.g. $\sigma_{AB} = 1.30$ (bold, pink), a different solid-solid transition feature is observed.

that some low energy minima when $\sigma_{AB} \leq 1.05$ are highly destabilised by the large dopant and some higher energy minima when $\sigma_{AB} \leq 1.05$ become stabilised. Thus the binary minima enumerated in Figure 3.6 are no longer the lowest-lying minima for binary systems with $\sigma_{AB} > 1.05$.

Calculations of T_{ss} using Equation (2.12) and corresponding heat capacity curves show that the doping of LJ_{38} with an atom exceeding size parameter $\sigma_{AB} = 1.05$ continues to yield a decrease in T_{ss} until the transition disappears around $\sigma_{AB} \approx 1.20$ (Figure 3.11). For $\sigma_{AB} > 1.20$, a new solid-solid feature appears. It appears that this phenomenon does not involve fcc geometries, because these structures will be highly destabilised for $\sigma_{AB} \gg 1.00$.

3.5 Summary

The incorporation of a dopant atom into LJ_{38} systematically shifts T_{ss} within the regime where an fcc to icosahedral solid-solid transition is observed ($0.98 \lesssim \sigma_{AB} \lesssim 1.20$). The shift is more sensitive for a smaller dopant and more gradual for a larger dopant. Tuning the 'stickiness' parameter ε_{AB} and using a larger dopant ($\sigma_{AB} \gg 1.20$) also produce interesting trends or features in the heat capacity, but are beyond the scope of the current study.

4 | LJ_{31}

The LJ_{31} cluster is investigated in the context of the LJ_{38} analysis in Chapter 3. Analogous T_{ss} trends are reported for binary LJ_{31} systems ($N_A = 1$, $N_B = 30$) for dopants with varied size and 'stickiness' parameters. The two-state approximation for the numerical calculation of T_{ss} (presented in Section 2.1.3) is shown to adequately reproduce trends in the heat capacity for binary LJ_{31} when each state is comprised of permutation-inversion isomers corresponding to only one homogeneous minimum.

4.1 The solid-solid transition

Like LJ_{38}, the homogeneous LJ_{31} cluster also features a double-funnel energy landscape. The LJ_{31} global minimum is characterised by a 13-atom icosahedral core within an 18-atom Mackay[66] overlayer.[54] LJ_{31} undergoes a solid-solid transition between the global minimum and $LJ_{31}^{(2)}$, which has the same icosahedral core but an anti-Mackay overlayer (Figure 4.1).[118] The solid-solid transition manifests as a sharp feature in the heat capacity preceding the broader melting peak (Figure 4.2).

The temperature of the LJ_{31} solid-solid transition between the Mackay and anti-Mackay minima can be approximated using Equation (2.12) where state α consists of only one minimum $i \equiv LJ_{31}^{(1)}$ and state $\beta \equiv j \equiv LJ_{31}^{(2)}$. This approximation gives $k_B T_{ss/\varepsilon} = 0.027$ and is in agreement with the temperature of the solid-solid transition peak in Figure 4.2, which was generated from the 1000 lowest minima of LJ_{31} (recall Section 2.2).

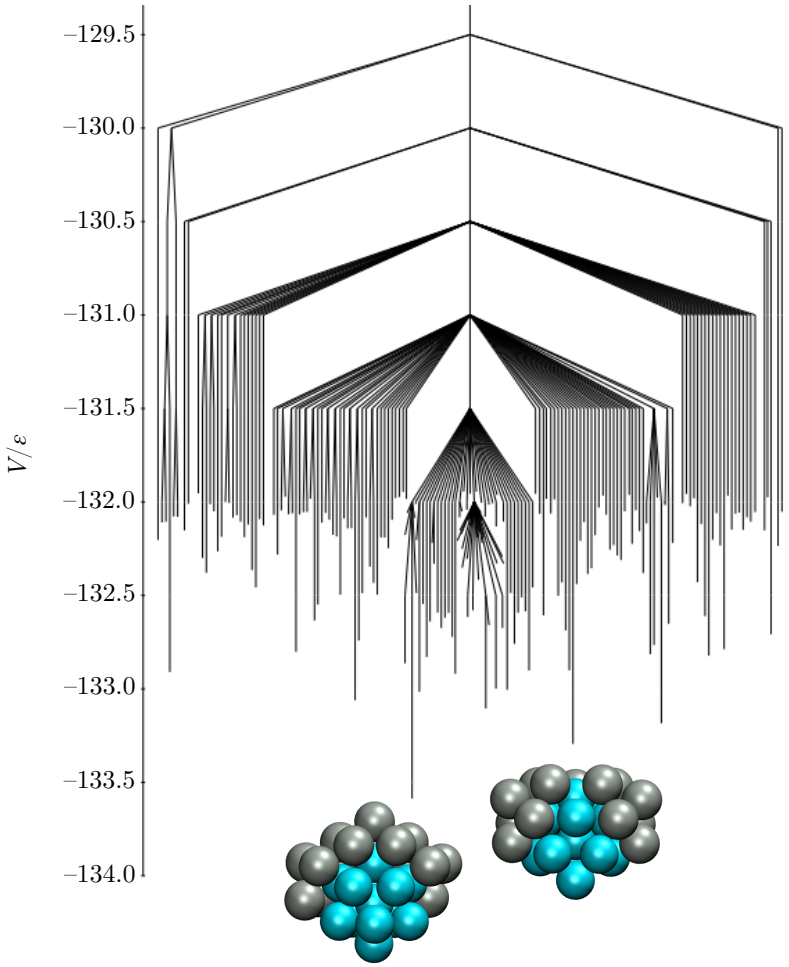

Figure 4.1: A disconnectivity graph for representative minima of the homogeneous LJ_{31} cluster.[118] A disconnectivity graph shows which minima are connected using pathways that lie below a series of energy thresholds.[118] The two lowest energy minima are shown, both of which have the same 13-atom icosahedral core (cyan). The 18-atom overlayer (grey) is either Mackay ($LJ_{31}^{(1)}$) or anti-Mackay ($LJ_{31}^{(2)}$).

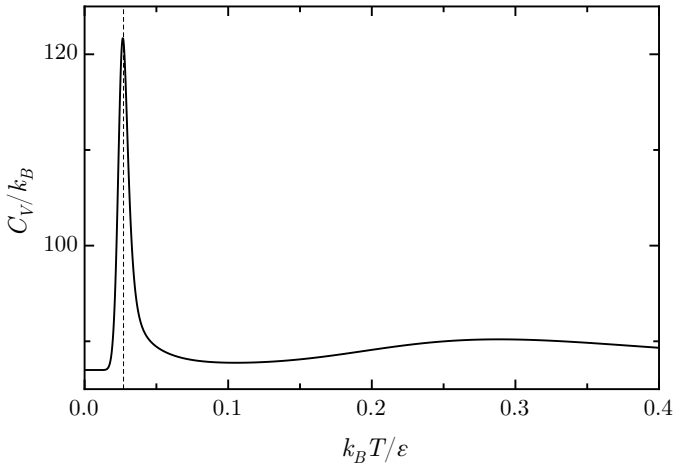

Figure 4.2: Constant volume heat capacity for homogeneous LJ_{31}. The broad peak at $k_BT/\varepsilon \approx 0.3$ represents the melting transition and the sharp peak represents the solid-solid transition. The dotted line at $k_BT/\varepsilon = 0.027$ indicates T_{ss} according to Equation (2.12) using the two lowest homogeneous minima.

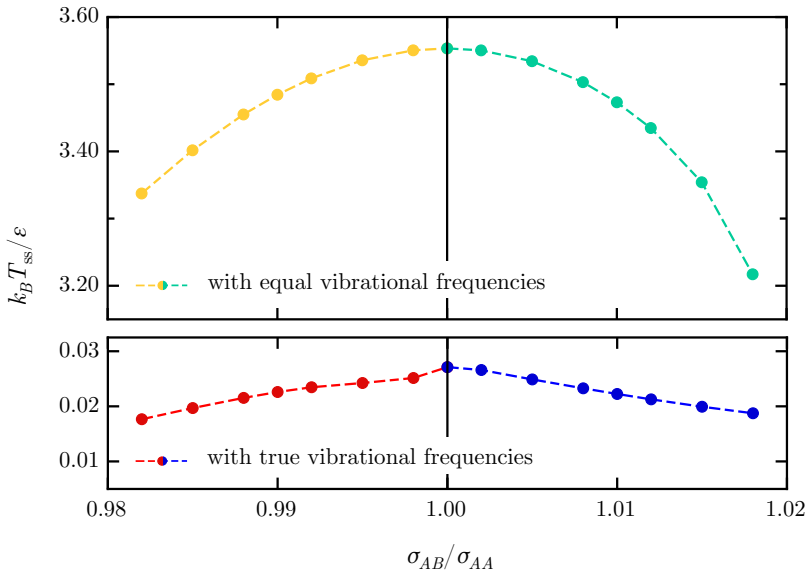

Figure 4.3: The solid-solid transition temperature of LJ_{31} as a function of the dopant size parameter σ_{AB}. The red and blue curve shows the true results, and the yellow and green curve shows the results when the vibrational frequencies are set to a constant value. For $\sigma_{AB} < 1.00$ (yellow and red), the lowest-lying structures feature the dopant atom on the interior of the cluster. For $\sigma_{AB} > 1.00$ (green and blue), the lowest-lying structures feature the dopant atom on the exterior of the cluster.

4.2 Dopant effects on the solid-solid transition

The exchange of a standard atom in the LJ_{31} cluster for a single impurity that differs only in its relative size ($N_A = 1$, $N_B = 30$; σ_{AB} is varied; $\sigma_{AA} = \sigma_{BB} = 1$; $\varepsilon_{AA} = \varepsilon_{AB} = \varepsilon_{BB} = 1$) is found to decrease T_{ss} for both larger and smaller impurities. As in Chapter 3, only small changes in dopant size are analysed ($0.95 \leq \sigma_{AB} \leq 1.05$). T_{ss} was calculated for the binary clusters as described in Section 4.1 for homogeneous LJ_{31}, where state α consists of the 20 permutation-inversion isomers of $LJ_{31}^{(1)}$ and state β consists of the 19 permutation-inversion isomers of $LJ_{31}^{(2)}$.

The incorporation of a dopant atom into LJ_{31} results in trends similar to those observed in LJ_{38} (Chapter 3). Binary systems with both larger and smaller dopant atoms exhibit a decrease in T_{ss} as the discrepancy of the dopant size parameter from 1.00 increases (Figure 4.3). When the global minimum switches to $LJ_{31}^{(2)}$ ($\sigma_{AB} \lesssim 0.96$), there is no apparent solid-solid transition between structurally distinct minima.

4.2.1 Vibrational entropy contribution

Potential energy, basin entropy (encoded by vibrational frequencies), and landscape entropy (encoded by point group orders) contribute to the free energy of a given minimum, and free energy relationships determine thermodynamic properties (recall Sections 2.1.3 and 3.2.1). For LJ_{38}, vibrational frequency parameters did not affect the trends observed in T_{ss} between fcc and icosahedral morphologies, so potential energy analyses could be extended to interpret free energy phenomena (see Figure 3.3 and Section 3.3). To assess the effect of basin entropy on T_{ss} trends in LJ_{31}, all values of T_{ss} were recalculated by replacing the true values of the vibrational frequencies in Equation (2.8) with a nonzero constant. The point group order o_i was retained.

The original and basin entropy controlled results are presented in Figure 4.3, which shows that the influence of the vibrational contribution is substantial. The removal of the basin entropy component from analysis results in a curve with a large offset that is more sensitive to changes in σ_{AB}. The offset is positive because the minima featuring an anti-Mackay overlayer have softer frequency modes than minima featuring a Mackay overlayer, which favours the transition to an anti-Mackay morphology via basin entropy.

4.3 Discussion

Doping LJ_{31} with an atom of a different size decreases T_{ss} between structures with different overlayers. Larger dopants prefer locations on the cluster exterior and smaller dopants prefer interior locations, which is consistent with dopant behaviour for LJ_{38} (see Section 3.4). Quantitative T_{ss} analyses are performed using permutation-inversion isomers of only the two lowest LJ_{31} minima (see Section 4.2), and heat capacity curves were produced from the permutation-inversion isomers of the 1000 lowest homogeneous LJ_{31} minima with one dopant atom (recall Section 2.2).

The incorporation of a larger dopant atom ($1.00 \leq \sigma_{AB} \leq 1.05$) into LJ_{31} produces a decrease in T_{ss} as σ_{AB} increases. This decrease is consistent with trends in the potential energy of the lowest-lying binary minima (Figure 4.4a), which show a decrease in the energy difference between the lowest-lying $LJ_{31}^{(1)}$ and $LJ_{31}^{(2)}$ structures as

σ_{AB} increases. The heat capacity curves resulting from incrementally larger values of σ_{AB} are illustrated in Figure 4.4b. Doping with a smaller atom ($0.95 \leq \sigma_{AB} \leq 1.00$) also produces a decrease in T_{ss} as σ_{AB} decreases until the global minimum switches to $\mathrm{LJ}_{31}^{(2)}$ ($\sigma_{AB} \lesssim 0.96$) (see Figure 4.5a). For $\sigma_{AB} \lesssim 0.96$, the heat capacity curve does not exhibit the sharp feature corresponding to the solid-solid transition between structures with Mackay and anti-Mackay overlayers (Figure 4.5b).

4.3.1 Permutation-inversion isomerisations

The heat capacity curves of doped LJ_{31} systems exhibit features that do not appear in the heat capacity of homogeneous LJ_{31} (see Figure 4.2). The very low temperatures of some of these transitions and their absence in the heat capacity of the homogeneous system indicate that they may correspond to permutation-inversion isomerisations. Unlike the isomerisation peaks identified in Section 3.4.3 for LJ_{38}, the binary system peaks in the LJ_{31} heat capacity are observed at temperatures both higher and lower than the solid-solid transition between geometrically distinct morphologies. The binary system features at low temperatures are presented in Figure 4.6, and features at $T > T_{\mathrm{ss}}(\text{Mackay} \rightarrow \text{anti-Mackay})$ are apparent in Figures 4.4b and 4.5b to the right of the more prominent transition between Mackay and anti-Mackay minima. T_{ss} for the Mackay $\rightarrow$ anti-Mackay transition and for the isomerisation features in Figures 4.4b, 4.5b, and 4.6 are presented in Figure 4.7 as functions of σ_{AB}. T_{ss} was taken as the temperature at the local maximum of the relevant feature in the heat capacity, and Equation (2.12) was not used.

4.3.2 Increasing the solid-solid transition temperature

The incorporation of a differently sized dopant atom into LJ_{31} has been shown to decrease the temperature of the solid-solid transition from a Mackay to an anti-Mackay minimum, but changes in σ_{AB} of the dopant have not been found to increase T_{ss}. Similar results were discussed for LJ_{38}, and an increase in $T_{\mathrm{ss}}(\text{fcc} \rightarrow \text{icos})$ was demonstrated for LJ_{38} by increasing the 'stickiness' parameter of the dopant atom and holding the size parameter constant at $\sigma_{AB} = 1.00$ (see Section 3.4.4). Increasing ε_{AB} at $\sigma_{AB} = 1.00$ for doped binary LJ_{31} produces analogous results and is shown to increase $T_{\mathrm{ss}}(\text{Mackay} \rightarrow \text{anti-Mackay})$ (Figure 4.8). T_{ss} was calculated using Equation (2.12)

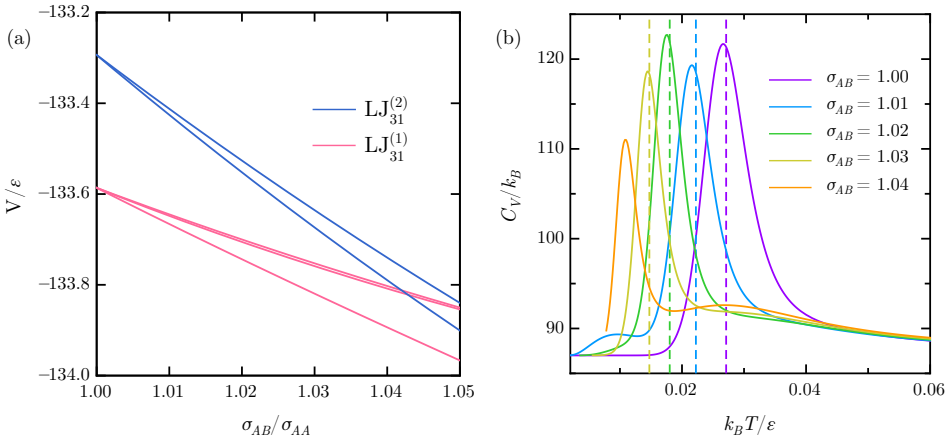

Figure 4.4: (a) The potential energy V of the lowest-lying minima of binary LJ_{31} for dopant radii $\sigma_{AB} > 1.00$. The set of minima shown is representative as opposed to complete. Different coloured curves indicate from which homogeneous minimum each binary structure is derived, and curves of the same colour intersect at $\sigma_{AB} = 1.00$, which represents the homogeneous structure. (b) The heat capacity of binary LJ_{31} for incrementally increasing values of σ_{AB} from 1.00 to 1.04. The solid-solid transition temperature shifts to the left as σ_{AB} increases. The dotted lines range from $k_BT/\varepsilon = 0.027$ (violet, $\sigma_{AB} = 1.00$) to 0.015 (gold, $\sigma_{AB} = 1.03$) and indicate k_BT_{ss}/ε for a given σ_{AB} value according to Equation (2.12) using all permutation-inversion isomers of the two lowest homogeneous minima. For $\sigma_{AB} > 1.03$, Equation (2.12) does not provide a meaningful T_{ss} value using only the two lowest homogeneous minima. The less prominent features on either side of the sharp peaks may represent permutation-inversion isomerisations.

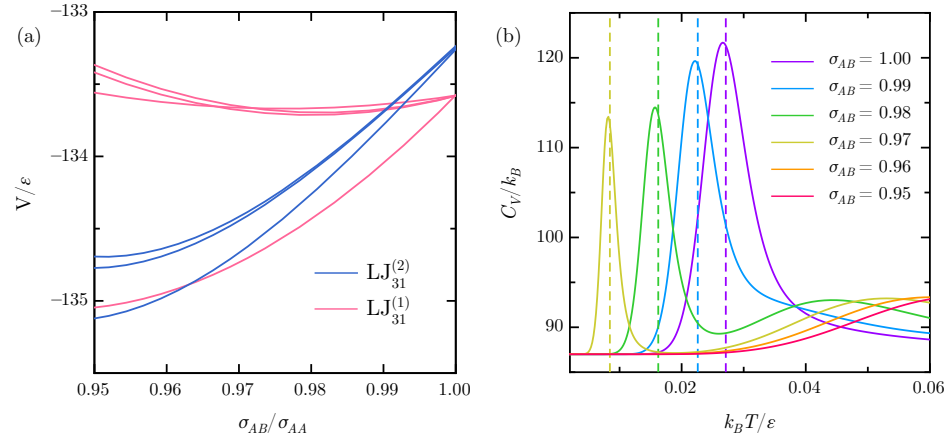

Figure 4.5: (a) The potential energy V of the lowest-lying minima of binary LJ_{31} for dopant radii $\sigma_{AB} < 1.00$. The set of minima shown is representative as opposed to complete. Different coloured curves indicate from which homogeneous minimum each binary structure is derived, and curves of the same colour intersect at $\sigma_{AB} = 1.00$, which represents the homogeneous structure. (b) The heat capacity of binary LJ_{31} for incrementally decreasing values of σ_{AB} from 1.00 to 0.95. The solid-solid transition temperature shifts to the left as σ_{AB} decreases but disappears for $\sigma_{AB} < 0.97$. The dotted lines range from $k_BT/\varepsilon = 0.027$ (violet, $\sigma_{AB} = 1.00$) to 0.008 (gold, $\sigma_{AB} = 0.97$) and indicate k_BT_{ss}/ε for a given σ_{AB} value according to Equation (2.12) using all permutation-inversion isomers of the two lowest homogeneous minima. The broader feature near $0.04 \lesssim k_BT/\varepsilon \lesssim 0.06$ may be a permutation-inversion isomerisation peak.

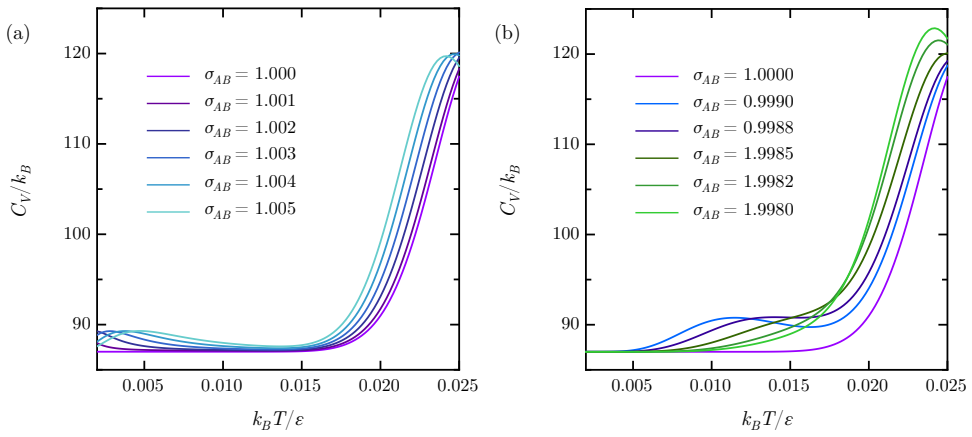

Figure 4.6: (a) The heat capacity of binary LJ_{31} for increasing values of σ_{AB} from 1.001 to 1.005. The small peak at low temperatures may represent a permutation-inversion isomerisation. The more prominent feature around $k_BT/\varepsilon \approx 0.03$ is the beginning of the solid-solid transition between Mackay and anti-Mackay morphologies (see Section 4.3). (b) The heat capacity of binary LJ_{31} for decreasing values of σ_{AB} from 1.000 to 0.998. The small peak at low temperatures may represent a permutation-inversion isomerisation. The more prominent feature around $k_BT/\varepsilon \approx 0.03$ is the beginning of the solid-solid transition between Mackay and anti-Mackay morphologies (see Section 4.3).

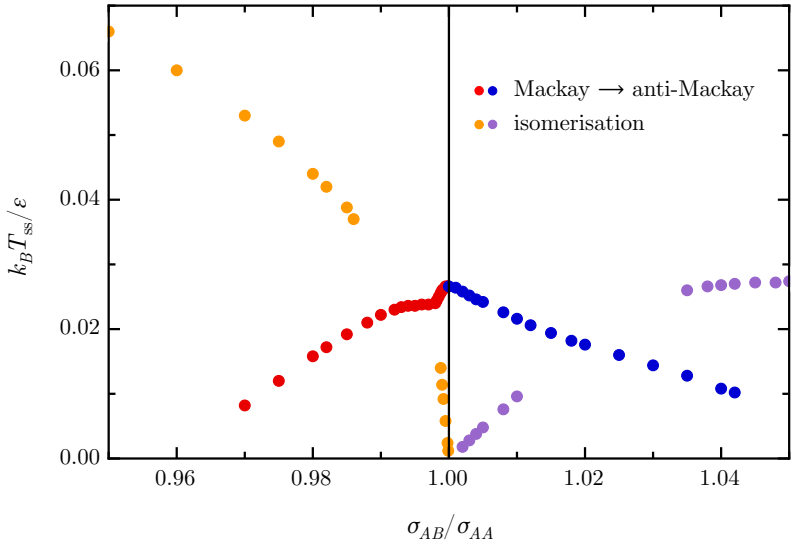

Figure 4.7: The structural and permutation-inversion isomerisation transition temperatures of LJ_{31} as functions of the dopant size parameter σ_{AB}. The red and blue circles represent the structural transition from Mackay to anti-Mackay morphologies, and the orange and violet circles represent transitions that appear only in the binary heat capacity curves, which probably correspond to permutation-inversion isomerisations. The isomerisation circles are coloured to suggest that the isomerisation features on either side of the Mackay → anti-Mackay transition represent the same phenomenon. The circles are coloured differently for $\sigma_{AB} > 1.00$ and $\sigma_{AB} < 1.00$ to indicate different processes for systems with dopant atoms of different relative sizes.

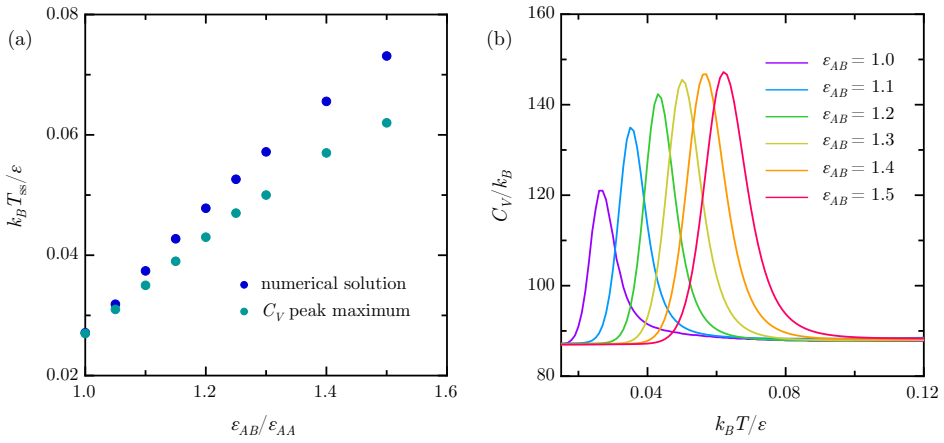

Figure 4.8: (a) The solid-solid transition temperature of LJ_{31} as a function of the dopant 'stickiness' parameter ε_{AB}. The blue circles show the numerical solutions of Equation (2.12) using all permutation-inversion isomers of the two lowest homogeneous minima, and teal circles indicate the local maxima of the solid-solid features in the heat capacity. (b) The heat capacity of binary LJ_{31} for increasing values of ε_{AB} from 1.0 to 1.5. The solid-solid transition temperature shifts to the right as ε_{AB} increases.

with the same α and β as in Section 4.2. In Figure 4.8a, this numerical result is compared with the k_BT/ε values at the local maximum of the solid-solid feature in the heat capacity. The numerical approximation using only $LJ_{31}^{(1-2)}$ produces the same trend observed in the heat capacity, but the accuracy of the approximation decreases systematically as ε_{AB} increases.

4.3.3 Approximations of T_{ss} using biminima

A biminimum structure represents a local minimum in both coordinate and permutation space.[122] In the context of a doped LJ system, the set of permutation-inversion isomers corresponding to a given homogeneous minimum contains one biminimum, which is the lowest energy isomer. In Section 4.2, T_{ss} for the Mackay $\rightarrow$ anti-Mackay transition of binary LJ_{31} was approximated using Equation (2.12) where the 20 permutation-inversion isomers of $LJ_{31}^{(1)}$ comprised state α and the 19 permutation-inversion isomers of $LJ_{31}^{(2)}$ comprised state β. This analysis was repeated using only the biminima of $LJ_{31}^{(1)}$ and $LJ_{31}^{(2)}$ to represent the solid states α and β of the system, respectively. The results show that the use of a single biminimum to represent each solid state reproduces the T_{ss} trend observed when including all corresponding permutation-inversion isomers (Figure 4.9).

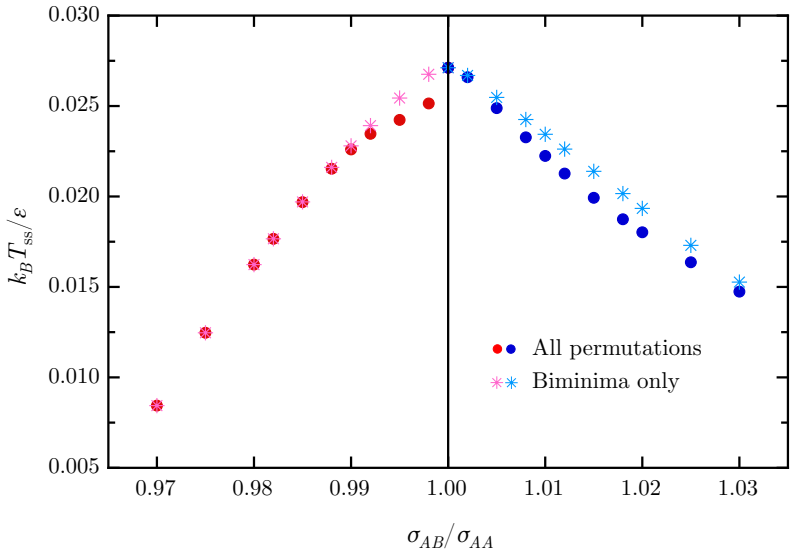

Figure 4.9: The solid-solid transition temperature of LJ_{31} as a function of the dopant size parameter σ_{AB}. The red and blue circles show the results using all permutation-inversion isomers of $LJ_{31}^{(1-2)}$, and the pink and light blue stars show the results using only the biminima of $LJ_{31}^{(1-2)}$. The circles and stars are coloured differently for $\sigma_{AB} > 1.00$ and $\sigma_{AB} < 1.00$ to indicate different processes for systems with dopant atoms of different relative sizes.

4.4 Summary

Incorporating a dopant atom into LJ_{31} decreases the temperature of the solid-solid transition from $LJ_{31}^{(1)}$ (Mackay overlayer) to $LJ_{31}^{(2)}$ (anti-Mackay overlayer) for small changes in dopant size ($0.96 \lesssim \sigma_{AB} \lesssim 1.04$). An increase in T_{ss}(Mackay $\rightarrow$ anti-Mackay) can be achieved by increasing the 'stickiness' parameter of the dopant atom ($\varepsilon_{AB} > 1.00$). T_{ss}(Mackay $\rightarrow$ anti-Mackay) can be approximated by assigning the permutation-inversion isomers of $LJ_{31}^{(1)}$ and $LJ_{31}^{(2)}$ to comprise states α and β, respectively. The trend in T_{ss} is reproduced by an even simpler approximation in which each solid state is represented only by the relevant biminimum, i.e. $\alpha \equiv i \equiv \text{bimin}\{LJ_{31}^{(1)}\}$ and $\beta \equiv j \equiv \text{bimin}\{LJ_{31}^{(2)}\}$.

For both LJ_{38} (see Chapter 3) and LJ_{31}, T_{ss} has been determined numerically by partitioning minima into two solid states and solving for the temperature at which the free energies of those states intersect (see Section 2.1.3). For the fcc $\rightarrow$ icos transition of LJ_{38} and the Mackay $\rightarrow$ anti-Mackay transition of LJ_{31}, numerical solutions for T_{ss} agree with features in the heat capacity. The numerical method relies on the choice of lumping criteria, and the results it produces are contextualised by that choice. For the analysis of LJ_{38} in Chapter 3, choosing only the global minimum to define state

α and allocating all other minima to state β produced satisfactory agreement with heat capacity features. For LJ_{31}, the use of only $LJ_{31}^{(1-2)}$ offered a straightforward lumping criterion and yielded agreement with the heat capacity, but determining how to allocate $LJ_{31}^{(i)}$, $i \geq 3$ is not trivial. It is also not straightforward to choose lumping criteria for minima involved in permutation-inversion isomerisations (see Sections 3.4.3 and 4.3.1). An exhaustive search of partitioning options for the three permutation-inversion isomers of $LJ_{38}^{(1)}$ did not produce T_{ss} values that consistently agreed with features observed in the heat capacity, which indicates a limitation of the two-state approximation.

5 | Conclusions

This thesis describes the solid-solid transitions exhibited by doped LJ_{38} and LJ_{31} systems and elucidates the competing potential energy effects that contribute to free energy behaviour. The sensitivity of these transitions to the size and 'stickiness' parameters of a single dopant atom enables tuning of the solid-solid transition temperature within the regime where the homogeneous global minimum is maintained. Furthermore, choosing a dopant atom outside of this regime changes the system global minimum, which offers a route for selecting the most stable geometric motif of a binary system. Changes in T_{ss} as a function of dopant size or 'stickiness' were calculated using a two-state approximation, which produced results in agreement with corresponding heat capacity signatures. It was demonstrated that the fidelity of the two-state approximation to trends in heat capacity features can be maintained when a single biminimum is chosen to represent each solid state.

The binary LJ potential was chosen to examine solid-solid transitions in order to provide a basis for future work using higher levels of theory or physical systems. The identification of regimes in which the presence of a dopant atom does not change the global minimum morphology can inform studies where the benefits of multicomponent nanoclusters, such as resistance to catalyst deactivation,[3,4] are desired without the structural changes that frequently accompany doping.[19] In summary, this thesis provides an account of solid-solid transitions in LJ clusters, and is intended to serve as a theoretical foundation for the programming of solid-solid transition behaviour in nanoalloys.

A | The harmonic approximation

A complete derivation of the harmonic approximation is presented. The harmonic approximation is a component of the HSA as described in Section 2.1. The HSA is utilised to extract thermodynamic observables (see Section 2.1.3) from a database of local minima. Consider a single minimum on the PES. The classical harmonic Hamiltonian for a system containing N particles in normal mode coordinates Q_α at this minimum is given by Equation (A.1). This minimum has potential energy V and $3N-6=\kappa$ vibrational degrees of freedom, and ω is the angular frequency associated with each normal mode α:

$$H = V + \frac{1}{2}\sum_{\alpha=1}^{\kappa}\left(\dot{Q}_\alpha^2 + \omega_\alpha^2 Q_\alpha^2\right). \tag{A.1}$$

The first term of the summation in Equation (A.1) ($\dot{Q}_\alpha^2$) refers to the momentum associated with each particle in the system, and the second term ($\omega_\alpha^2 Q_\alpha^2$) refers to the configurational energy of the system. The configurational partition function for the basin of the relevant minimum in normal mode coordinates is given by

$$Z_c(\beta) = \frac{1}{\prod_{\alpha=1}^{N} M_\alpha^{3/2}} \int\int\cdots\int_{-\infty}^{\infty} e^{-\beta H_c(Q_\alpha)}\,\mathrm{d}Q_1\,\mathrm{d}Q_2\cdots\mathrm{d}Q_\kappa, \tag{A.2}$$

where β is defined as $1/k_BT$, $H_c(Q_\alpha) = V + \frac{1}{2}\sum_{\alpha=1}^{\kappa}\omega_\alpha^2 Q_\alpha^2$ is the configurational part of the Hamiltonian, and the term preceding the integral is the Jacobian factor produced by the change of variables to normal mode coordinates. This factor requires atomic masses, which are assumed to be identical for all LJ atoms. The harmonic oscillator at each coordinate Q_α is considered to be independent of the oscillators at all other coordinates, so Equation (A.2) can be rewritten where the multiple integral is replaced with the product of definite integrals:

$$Z_c(\beta) = \frac{e^{-\beta V}}{\prod_{\alpha=1}^{N} M_\alpha^{3/2}} \prod_{\alpha=1}^{\kappa} \int_{-\infty}^{\infty} e^{-\frac{\beta}{2}\omega_\alpha^2 Q_\alpha^2} \, \mathrm{d}Q_\alpha. \tag{A.3}$$

Since $\int_{-\infty}^{\infty} \exp(-\beta\omega_\alpha^2 Q_\alpha^2/2) \, \mathrm{d}Q_\alpha = \sqrt{2\pi/\beta\omega_\alpha^2}$, Equation (A.3) can be further reduced to

$$Z_c(\beta) = \frac{e^{-\beta V} \beta^{-\kappa/2}}{(2\pi)^{\kappa/2} \prod_{\alpha=1}^{N} M_\alpha^{3/2}} \prod_{\alpha=1}^{\kappa} \frac{2\pi}{\omega_\alpha}, \tag{A.4}$$

where $\nu_\alpha = \omega_\alpha/2\pi$ is the vibrational frequency of mode α. For geometric mean vibrational frequency $\overline{\nu}$, note that $\overline{\nu}^\kappa = \prod_{\alpha=1}^{\kappa} \nu_\alpha$. Equation (A.4) can thus be written as Equation (A.5), where the configurational partition function Z_c of a single basin is expressed using the harmonic approximation:

$$Z_c(\beta) = \frac{e^{-\beta V} \beta^{-\kappa/2}}{(2\pi)^{\kappa/2} \overline{\nu}^\kappa \prod_{\alpha=1}^{N} M_\alpha^{3/2}}. \tag{A.5}$$

The partition function for the momentum part of the Hamiltonian can be derived in an analogous fashion using Jacobian factor $\prod_{\alpha=1}^{N} M_\alpha^{3/2}$ and differentiating with respect to $\dot{Q}_\alpha$, which gives:

$$Z_m(\beta) = \frac{(2\pi)^{\kappa/2} \prod_{\alpha=1}^{N} M_\alpha^{3/2}}{\beta^{\kappa/2}}. \tag{A.6}$$

The partition function is related to the density of states of the system by the Laplace transform

$$Z(\beta) = \mathcal{L}\{\Omega(E)\} = \int_0^\infty \Omega(E) e^{-\beta E} \, \mathrm{d}E, \tag{A.7}$$

so in order to obtain the density of states from the partition functions in Equations (A.5) and (A.6) the inverse Laplace transform can be applied to Z_c and Z_m. Furthermore, applying the first integration theorem of the Laplace transformation to the partition function gives the relation:[123]

$$\frac{Z_c(\beta)}{\beta} = \mathcal{L}\left\{ \int_0^E \Omega_c(\epsilon) \, \mathrm{d}\epsilon \right\}. \tag{A.8}$$

Since the integral to which the Laplace transform is applied is equal to the volume

$G_c(E)$, the inverse Laplace transform can be performed on both Z_c and Z_c/β to give the configurational density of states and the phase space volume, respectively:

$$\Omega_c(E) = \mathcal{L}^{-1}\{Z_c(\beta)\} = \frac{(E_c - V)^{\kappa/2-1}\Theta[E-V]}{(2\pi)^{\kappa/2}\Gamma(\kappa/2)\overline{\nu}^{\kappa}\prod_{\alpha=1}^{N} M_\alpha^{3/2}}, \tag{A.9a}$$

$$G_c(E) = \mathcal{L}^{-1}\left\{\frac{Z_c(\beta)}{\beta}\right\} = \frac{(E_c - V)^{\kappa/2}\Theta[E-V]}{(2\pi)^{\kappa/2}\Gamma(\kappa/2+1)\overline{\nu}^{\kappa}\prod_{\alpha=1}^{N} M_\alpha^{3/2}}, \tag{A.9b}$$

where the Heaviside step function $\Theta[x] = \frac{1}{2}(1 + \mathrm{sgn}(x))$ is included because Ω_c and G_c vanish unless $E > V$.

An analogous procedure can be performed for the momentum partition function to yield Equations (A.10a) and (A.10b), which represent the density of states and phase space volume associated with the momentum, respectively:

$$\Omega_m(E) = \mathcal{L}^{-1}\{Z_m(\beta)\} = \frac{(2\pi)^{\kappa/2}E_m^{\kappa/2-1}\prod_{\alpha=1}^{N} M_\alpha^{3/2}}{\Gamma(\kappa/2)}, \tag{A.10a}$$

$$G_m(E) = \mathcal{L}^{-1}\left\{\frac{Z_m(\beta)}{\beta}\right\} = \frac{(2\pi)^{\kappa/2}E_m^{\kappa/2}\prod_{\alpha=1}^{N} M_\alpha^{3/2}}{\Gamma(\kappa/2+1)}. \tag{A.10b}$$

The total density of states Ω is obtained by the inverse Laplace transform of the product of the two partition functions Z_c and Z_m. Applying the convolution theorem for the Laplace transform gives

$$\mathcal{L}^{-1}\{Z_c Z_m\} = \Omega(E) = \int_V^E \Omega_c(E_c)\Omega_m(E - E_c)\,\mathrm{d}E_c, \tag{A.11}$$

which can be solved to yield the density of states Ω and subsequently integrated to produce its antiderivative, the phase space volume G:[a]

$$\Omega(E) = \frac{(E-V)^{\kappa-1}\Theta[E-V]}{\Gamma(\kappa)\overline{\nu}^{\kappa}}, \tag{A.12a}$$

$$G(E) = \frac{(E-V)^{\kappa}\Theta[E-V]}{\Gamma(\kappa+1)\overline{\nu}^{\kappa}}. \tag{A.12b}$$

Equation (A.12a) can be adapted to describe the density of states for the entire system as the sum of contributions from each individual, geometrically distinct basin for all

[a]Though the Jacobian factors containing atomic mass information cancel in the product in Equation (A.11), they have influenced the vibrational frequencies that remain in Ω_c and Ω_m.

minima with potential energy $V_\mathrm{a} < E$,

$$\Omega(E) = \sum_{V_\mathrm{a}<E} \frac{n_\mathrm{a}(E - V_\mathrm{a})^{\kappa-1}}{\Gamma(\kappa)(h\overline{\nu}_\mathrm{a})^{\kappa}}, \tag{A.13}$$

where n_a is incorporated to account for permutation-inversion isomers (see Section 2.1.1), h is Planck's constant, and $1/h^{\kappa}$ is included to maintain agreement with the classical limit of quantum statistical mechanics.[109]

Finally, the corresponding partition function for the canonical ensemble can be calculated from the Laplace transform of Ω (see Equation (A.7)):

$$Z(\beta) = \sum_\mathrm{a} \frac{n_\mathrm{a} e^{-\beta V_\mathrm{a}}}{(\beta h\overline{\nu}_\mathrm{a})^{\kappa}}. \tag{A.14}$$

B | Strain energy

The presence of a larger or smaller dopant atom in an LJ cluster causes the dopant nearest neighbour distances to deviate from the equilibrium pair distances. This deviation results in a local energetic penalty V_{strain} for the structure,[119,120] which is defined as

$$V_{\text{strain}} = V_{\text{nn}} + \varepsilon N_{\text{nn}}. \tag{B.1}$$

For a single impurity LJ system, $\varepsilon = \varepsilon_{AB}$ and V_{nn} is given by

$$V_{\text{nn}} = 4 \sum_{\substack{\text{neighbours} \\ \text{of } A}} \varepsilon_{AB} \left[\left(\frac{\sigma_{AB}}{r} \right)^{12} - \left(\frac{\sigma_{AB}}{r} \right)^{6} \right], \tag{B.2}$$

where r is the distance between the dopant atom A and neighbouring atom B, and σ_{AB} and ε_{AB} are parameters of the binary LJ potential (see Equation (1.3)).

V_{nn}, and therefore V_{strain}, depends on the size parameter of the dopant atom. For the three permutation-inversion isomers of binary $\text{LJ}_{38}^{(1)}$, V_{strain} is calculated using Equation (B.1) for values of σ_{AB} between 0.95 and 1.05. All three isomers have fcc packing environments and differ only in the number of neighbours around the dopant N_{nn}. V_{strain} values are shown to be more sensitive to fcc structures with higher N_{nn} (Figure B.1). The relative shapes of the strain energy curves resemble those corresponding to the potential energies of the same structures (see Figure 3.4).

The sensitivity of V_{strain} to changes in σ_{AB} also depends on the local packing environment of the dopant atom. The low-lying minima of binary LJ_{38} feature dopant atoms within fcc, icosahedral, and Ino-dodecahedral packing environments with various N_{nn} (see Sections 3.3.1 and 3.3.2). Equation (B.1) was used to calculate V_{strain} for the low-lying binary minima of LJ_{38} (see Figure 3.6) for values of σ_{AB} between 0.95

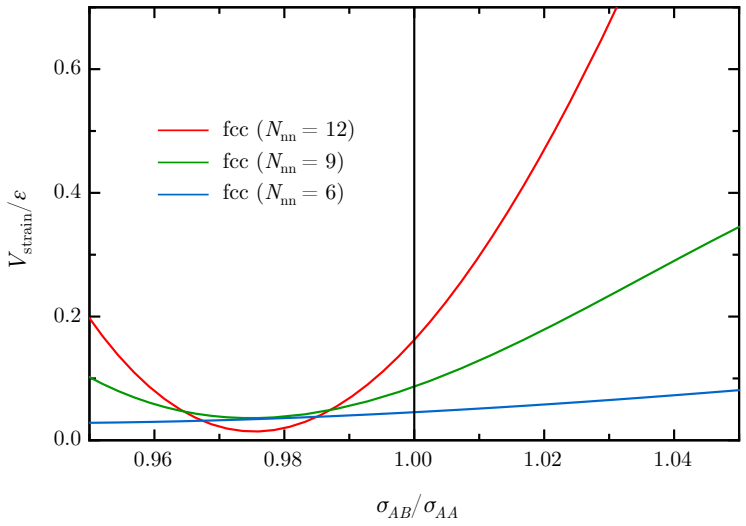

Figure B.1: Strain energy V_{strain} induced by a dopant atom for the three permutation-inversion isomers of $\mathrm{LJ}_{38}^{(1)}$ for dopant size parameters $0.95 \leq \sigma_{AB} \leq 1.05$. $\sigma_{AB} = 1.00$ represents the homogeneous structure, where the only distinction between the dopant atom and its neighbours is the atom type label. The relative shapes of the curves resemble the corresponding potential energy curves presented in Figure 3.4.

and 1.05. For all dopant packing environments, binary minima with small dopants ($\sigma_{AB} \approx 0.95$) exhibit low V_{strain}. In general, V_{strain} increases with increasing σ_{AB}, with the exception of minima containing the dopant atom within an incomplete Ino-dodecahedral neighbour environment ($N_{\mathrm{nn}} \in \{6, 7, 8\}$), where V_{strain} is not significantly affected by changes in σ_{AB}. Figure B.2 shows the strain energies of representative low-lying minima of binary LJ_{38} as a function of σ_{AB}. The relative shapes of the strain energy curves resemble those corresponding to the potential energies of the same structures (see Figure 3.5).

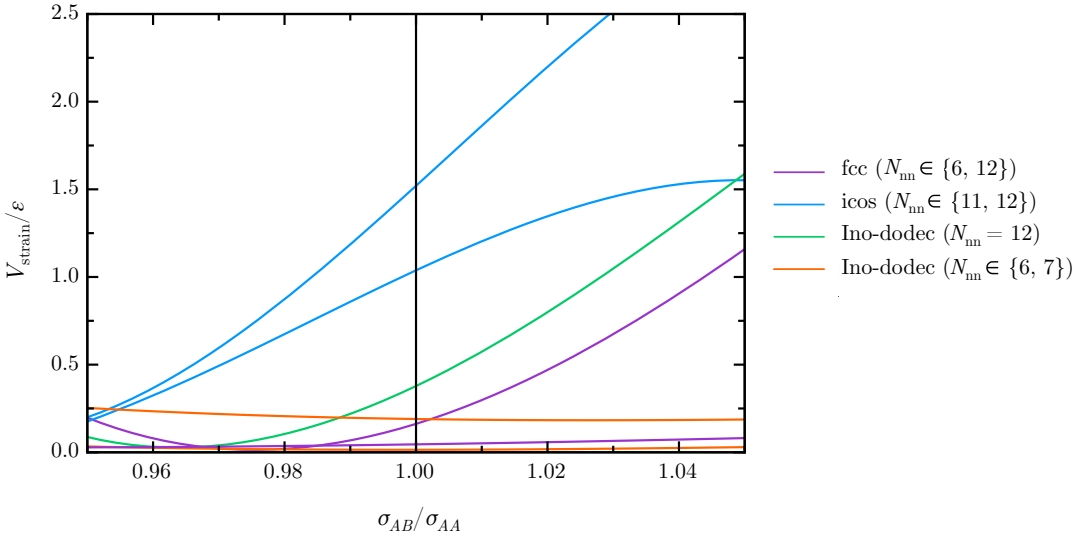

Figure B.2: Strain energy V_{strain} of representative low-lying binary LJ_{38} minima for dopant size parameters $0.95 \leq \sigma_{AB} \leq 1.05$. Different dopant packing environments are indicated with different colours on the graph. $\sigma_{AB} = 1.00$ represents the homogeneous structure, where the only distinction between the dopant atom and its neighbours is the atom type label. The relative shapes of the curves resemble the corresponding potential energy curves presented in Figure 3.5. The V_{strain} values used to calculate curve thicknesses for Figure 3.5 are evaluated at $\sigma_{AB} = 1.00$.

References

[1] Sun, S.; Murray, C. B.; Weller, D.; Folks, L.; Moser, A. *Science* **2000**, *287*, 1989–1992.

[2] Shipway, A. N.; Katz, E.; Willner, I. *ChemPhysChem* **2000**, *1*, 18–52.

[3] Molenbroek, A. M.; Nørskov, J. K.; Clausen, B. S. *J. Phys. Chem. B* **2001**, *105*, 5450–5458.

[4] Arrii, S.; Morfin, F.; Renouprez, A. J.; Rousset, J. L. *J. Am. Chem. Soc.* **2004**, *126*, 1199–1205.

[5] Loo, C.; Lowery, A.; Halas, N.; West, J.; Drezek, R. *Nano Lett.* **2005**, *5*, 709–711.

[6] Seo, W. S.; Lee, J. H.; Sun, X.; Suzuki, Y.; Mann, D.; Liu, Z.; Terashima, M.; Yang, P. C.; McConnell, M. V.; Nishimura, D. G.; Dai, H. *Nat. Mater.* **2006**, *5*, 971–976.

[7] Huang, X.; Jain, P. K.; El-Sayed, I. H.; El-Sayed, M. A. *Nanomedicine* **2007**, *2*, 681–693.

[8] Ferrando, R.; Jellinek, J.; Johnston, R. L. *Chem. Rev.* **2008**, *108*, 845–910.

[9] Nel, A. E.; Madler, L.; Velegol, D.; Xia, T.; Hoek, E. M. V.; Somasundaran, P.; Klaessig, F.; Castranova, V.; Thompson, M. *Nat. Mater.* **2009**, *8*, 543–557.

[10] Jellinek, J.; Krissinel, E. *Chem. Phys. Lett.* **1996**, *258*, 283–292.

[11] Darby, S.; Mortimer-Jones, T. V.; Johnston, R. L.; Roberts, C. *J. Chem. Phys.* **2002**, *116*, 1536–1550.

[12] Rossi, G.; Rapallo, A.; Mottet, C.; Fortunelli, A.; Baletto, F.; Ferrando, R. *Phys. Rev. Lett.* **2004**, *93*, 105503.

[13] Mottet, C.; Rossi, G.; Baletto, F.; Ferrando, R. *Phys. Rev. Lett.* **2005**, *95*, 035501.

[14] Calvo, F.; Yurtsever, E. *Phys. Rev. B* **2004**, *70*, 045423.

[15] Doye, J. P. K.; Meyer, L. *Phys. Rev. Lett.* **2005**, *95*, 063401.

[16] Aguado, A.; González, L. E.; López, J. M. *J. Phys. Chem. B* **2004**, *108*, 11722–11731.

[17] Aguado, A.; López, J. M. *Phys. Rev. B* **2005**, *72*, 205420.

[18] Rossi, G.; Ferrando, R.; Rapallo, A.; Fortunelli, A.; Curley, B. C.; Lloyd, L. D.; Johnston, R. L. *J. Chem. Phys.* **2005**, *122*, 194309.

[19] Rapallo, A.; Rossi, G.; Ferrando, R.; Fortunelli, A.; Curley, B. C.; Lloyd, L. D.; Tarbuck, G. M.; Johnston, R. L. *J. Chem. Phys.* **2005**, *122*, 194308.

[20] Chandrachud, P.; Joshi, K.; Kanhere, D. G. *Phys. Rev. B* **2007**, *76*, 235423.

[21] Jiang, A.; Awasthi, N.; Kolmogorov, A. N.; Setyawan, W.; Börjesson, A.; Bolton, K.; Harutyunyan, A. R.; Curtarolo, S. *Phys. Rev. B* **2007**, *75*, 205426.

[22] Hock, C.; Straßburg, S.; Haberland, H.; v. Issendorff, B.; Aguado, A.; Schmidt, M. *Phys. Rev. Lett.* **2008**, *101*, 023401.

[23] Calvo, F.; Cottancin, E.; Broyer, M. *Phys. Rev. B* **2008**, *77*, 121406.

[24] Arslan, H.; Irmak, A. E. *Int. J. Mod. Phys. C* **2009**, *20*, 1737–1747.

[25] Aguado, A.; López, J. M. *J. Chem. Phys.* **2010**, *133*, 094302.

[26] Rapallo, A.; Olmos-Asar, J. A.; Oviedo, O. A.; Ludueña, M.; Ferrando, R.; Mariscal, M. M. *J. Phys. Chem. C* **2012**, *116*, 17210–17218.

[27] Lyalin, A.; Hussien, A.; Solov'yov, A. V.; Greiner, W. *Phys. Rev. B* **2009**, *79*, 165403.

[28] Marks, L. D. *Rep. Prog. Phys.* **1994**, *57*, 603.

[29] Jones, J. E.; Ingham, A. E. *Proc. R. Soc. London Ser. A* **1925**, *107*, 636–653.

[30] Nauchitel, V.; Pertsin, A. *Mol. Phys.* **1980**, *40*, 1341–1355.

[31] Wales, D. J.; Doye, J. P. K. *J. Phys. Chem. A* **1997**, *101*, 5111–5116.

[32] Doye, J. P. K.; Wales, D. J.; Miller, M. A. *J. Chem. Phys.* **1998**, *109*, 8143–8153.

[33] Doye, J. P. K.; Wales, D. J. *Phys. Rev. Lett.* **1998**, *80*, 1357–1360.

[34] Calvo, F.; Doye, J. P. K. *Phys. Rev. E* **2000**, *63*, 010902.

[35] Calvo, F.; Neirotti, J. P.; Freeman, D. L.; Doll, J. D. *J. Chem. Phys.* **2000**, *112*, 10350–10357.

[36] Neirotti, J. P.; Calvo, F.; Freeman, D. L.; Doll, J. D. *J. Chem. Phys.* **2000**, *112*, 10340–10349.

[37] Frantz, D. D. *J. Chem. Phys.* **2001**, *115*, 6136–6157.

[38] Sabo, D.; Freeman, D. L.; Doll, J. D. *J. Chem. Phys.* **2005**, *122*, 094716.

[39] Liu, H.; Jordan, K. D. *J. Phys. Chem. A* **2005**, *109*, 5203–5207.

[40] Mandelshtam, V. A.; Frantsuzov, P. A.; Calvo, F. *J. Phys. Chem. A* **2006**, *110*, 5326–5332.

[41] Sharapov, V. A.; Mandelshtam, V. A. *J. Phys. Chem. A* **2007**, *111*, 10284–10291.

[42] Mie, G. *Ann. Phys. (Berlin)* **1903**, *316*, 657–697.

[43] Rosenbluth, M. N.; Rosenbluth, A. W. *J. Chem. Phys.* **1954**, *22*, 881–884.

[44] Metropolis, N.; Rosenbluth, A. W.; Rosenbluth, M. N.; Teller, A. H.; Teller, E. *J. Chem. Phys.* **1953**, *21*, 1087–1092.

[45] Wood, W. W.; Parker, F. R. *J. Chem. Phys.* **1957**, *27*, 720–733.

[46] Hoare, M.; Pal, P. *Adv. Phys.* **1971**, *20*, 161–196.

[47] Hoare, M.; Pal, P. *Nat. Phys. Sci.* **1971**, *230*, 5–8.

[48] Hoare, M.; Pal, P. *Nat. Phys. Sci.* **1972**, *236*, 35–37.

[49] Hoare, M.; Pal, P. *Adv. Phys.* **1975**, *24*, 645–678.

[50] Hoare, M. *Adv. Chem. Phys.*; John Wiley & Sons, Inc., 1979; Vol. 40; pp 49–135.

[51] Freeman, D. L.; Doll, J. D. *J. Chem. Phys.* **1985**, *82*, 462–471.

[52] Farges, J.; Feraudy, M. D.; Raoult, B.; Torchet, G. *Surf. Sci.* **1985**, *156*, 370–378.

[53] Wille, L. *Chem. Phys. Lett.* **1987**, *133*, 405–410.

[54] Northby, J. A. *J. Chem. Phys.* **1987**, *87*, 6166–6177.

[55] Coleman, T.; Shalloway, D.; Wu, Z. *J. Global Optim.* **1994**, *4*, 171–185.

[56] Xue, G. *J. Global Optim.* **1994**, *4*, 425–440.

[57] Pillardy, J.; Piela, L. *J. Phys. Chem.* **1995**, *99*, 11805–11812.

[58] Doye, J. P. K.; Wales, D. J.; Berry, R. S. *J. Chem. Phys.* **1995**, *103*, 4234–4249.

[59] Doye, J. P. K.; Wales, D. J. *Chem. Phys. Lett.* **1995**, *247*, 339–347.

[60] Barrón, C.; Gómez, S.; Romero, D. *Appl. Math. Lett.* **1996**, *9*, 75–78.

[61] Deaven, D.; Tit, N.; Morris, J.; Ho, K. *Chem. Phys. Lett.* **1996**, *256*, 195–200.

[62] Barrón, C.; Gómez, S.; Romero, D. *Appl. Math. Lett.* **1997**, *10*, 25–28.

[63] Leary, R. *J. Global Optim.* **1997**, *11*, 35–53.

[64] Barrón, C.; Gómez, S.; Romero, D.; Saavedra, A. *Appl. Math. Lett.* **1999**, *12*, 85–90.

[65] Leary, R. H. Abstract for the *International Workshop on Global Optimization*; 1999.

[66] Mackay, A. L. *Acta Crystallogr.* **1962**, *15*, 916–918.

[67] Marks, L. D. *Philos. Mag. A* **1984**, *49*, 81–93.

[68] Burton, J. J. *J. Chem. Phys.* **1970**, *52*, 345–352.

[69] Burton, J. J. *Nature* **1971**, *229*, 335–336.

[70] McGinty, D. J. *J. Chem. Phys.* **1973**, *58*, 4733–4742.

[71] Kristensen, W. D.; Jensen, E. J.; Cotterill, R. M. J. *J. Chem. Phys.* **1974**, *60*, 4161–4169.

[72] Briant, C. L.; Burton, J. J. *J. Chem. Phys.* **1975**, *63*, 2045–2058.

[73] Farges, J.; De Feraudy, M. F.; Raoult, B.; Torchet, G. *J. Phys. Colloques* **1977**, *38*, C2–47–C2–51.

[74] Lee, J. K.; Barker, J. A.; Abraham, F. F. *J. Chem. Phys.* **1973**, *58*, 3166–3180.

[75] Etters, R. D.; Kaelberer, J. *Phys. Rev. A* **1975**, *11*, 1068–1079.

[76] Kaelberer, J. B.; Etters, R. D. *J. Chem. Phys.* **1977**, *66*, 3233–3239.

[77] Etters, R. D.; Danilowicz, R.; Dugan, J. *J. Chem. Phys.* **1977**, *67*, 1570–1575.

[78] Quirke, N.; Sheng, P. *Chem. Phys. Lett.* **1984**, *110*, 63 – 66.

[79] Jellinek, J.; Beck, T. L.; Berry, R. S. *J. Chem. Phys.* **1986**, *84*, 2783–2794.

[80] Davis, H. L.; Jellinek, J.; Berry, R. S. *J. Chem. Phys.* **1987**, *86*, 6456–6464.

[81] Honeycutt, J. D.; Andersen, H. C. *J. Phys. Chem.* **1987**, *91*, 4950–4963.

[82] Beck, T. L.; Berry, R. S. *J. Chem. Phys.* **1988**, *88*, 3910–3922.

[83] Berry, R. S.; Beck, T. L.; Davis, H. L.; Jellinek, J. *Adv. Chem. Phys.*; John Wiley & Sons, Inc., 1988; Vol. 70; pp 75–138.

[84] Labastie, P.; Whetten, R. L. *Phys. Rev. Lett.* **1990**, *65*, 1567–1570.

[85] Cheng, H.-P.; Li, X.; Whetten, R. L.; Berry, R. S. *Phys. Rev. A* **1992**, *46*, 791–800.

[86] Marinari, E.; Parisi, G. *Europhys. Lett.* **1992**, *19*, 451–458.

[87] Geyer, C. J.; Thompson, E. A. *J. Am. Stat. Assoc.* **1995**, *90*, 909–920.

[88] Hukushima, K.; Nemoto, K. *J. Phys. Soc. Jpn.* **1996**, *65*, 1604–1608.

[89] McGinty, D. J. *J. Chem. Phys.* **1971**, *55*, 580–588.

[90] Burton, J. J. *J. Chem. Phys.* **1972**, *56*, 3133–3138.

[91] Hoover, W. G.; Hindmarsh, A. C.; Holian, B. L. *J. Chem. Phys.* **1972**, *57*, 1980–1985.

[92] Burton, J. J. *J. Chem. Soc., Faraday Trans. 2* **1973**, *69*, 540–550.

[93] Tsai, N.-H.; Abraham, F. F.; Pound, G. *Surf. Sci.* **1978**, *77*, 465–492.

[94] Adams, J. E.; Stratt, R. M. *J. Chem. Phys.* **1990**, *93*, 1358–1368.

[95] Lopez, G. E.; Freeman, D. L. *J. Chem. Phys.* **1993**, *98*, 1428–1435.

[96] Garzón, I.; Long, X.; Kawai, R.; Weare, J. *Chem. Phys. Lett.* **1989**, *158*, 525–530.

[97] Clarke, A. S.; Kapral, R.; Moore, B.; Wu, X.-G. *Phys. Rev. Lett.* **1993**, *70*, 3283–3286.

[98] Clarke, A. S.; Kapral, R.; Patey, G. N. *J. Chem. Phys.* **1994**, *101*, 2432–2445.

[99] Frantz, D. D. *J. Chem. Phys.* **1996**, *105*, 10030–10049.

[100] Frantz, D. D. *J. Chem. Phys.* **1997**, *107*, 1992–2011.

[101] Sabo, D.; Doll, J. D.; Freeman, D. L. *J. Chem. Phys.* **2003**, *118*, 7321–7328.

[102] Sabo, D.; Doll, J. D.; Freeman, D. L. *J. Chem. Phys.* **2004**, *121*, 847–855.

[103] Sabo, D.; Predescu, C.; Doll, J. D.; Freeman, D. L. *J. Chem. Phys.* **2004**, *121*, 856–867.

[104] Frantz, D. D.; Freeman, D. L.; Doll, J. D. *J. Chem. Phys.* **1990**, *93*, 2769–2784.

[105] Bytheway, I.; Kepert, D. *J. Math. Chem.* **1992**, *9*, 161–180.

[106] Munro, L. J.; Tharrington, A.; Jordan, K. D. *Comput. Phys. Commun.* **2002**, *145*, 1–23.

[107] Quesada, N.; Moyano, G. E. *Phys. Rev. B* **2010**, *82*, 054104.

[108] Wales, D. J. *Mol. Phys.* **1993**, *78*, 151–171.

[109] Wales, D. J. *Energy Landscapes with Applications to Clusters, Biomolecules and Glasses*; Cambridge University Press, 2003.

[110] Doye, J. P. K.; Wales, D. J. *J. Chem. Phys.* **1995**, *102*, 9659–9672.

[111] Doye, J. P. K.; Calvo, F. *J. Chem. Phys.* **2002**, *116*, 8307–8317.

[112] Schebarchov, D. Department of Chemistry, University of Cambridge, UK. Personal communication, July 2015.

[113] Doye, J. P. K.; Miller, M. A.; Wales, D. J. *J. Chem. Phys.* **1999**, *110*, 6896–6906.

[114] Miller, M. A.; Doye, J. P. K.; Wales, D. J. *Phys. Rev. E* **1999**, *60*, 3701–3718.

[115] Rowley, L.; Nicholson, D.; Parsonage, N. *J. Comput. Phys.* **1975**, *17*, 401–414.

[116] Czerminski, R.; Elber, R. *J. Chem. Phys.* **1990**, *92*, 5580–5601.

[117] Becker, O. M.; Karplus, M. *J. Chem. Phys.* **1997**, *106*, 1495–1517.

[118] Doye, J. P. K.; Miller, M. A.; Wales, D. J. *J. Chem. Phys.* **1999**, *111*, 8417–8428.

[119] Doye, J. P. K.; Wales, D. J. *J. Phys. B: At. Mol. Opt. Phys.* **1996**, *29*, 4859.

[120] Doye, J. P. K.; Wales, D. J. *Science* **1996**, *271*, 484–487.

[121] Parneix, P.; Bréchignac, P.; Calvo, F. *Chem. Phys. Lett.* **2003**, *381*, 471–478.

[122] Schebarchov, D.; Wales, D. J. *Phys. Rev. Lett.* **2014**, *113*, 156102.

[123] Martiniani, S. Superposition Enhanced Nested Sampling. M.Phil. thesis, University of Cambridge, 2013.